

Selection of temporary storage strategy and description of uncertain parameters or processes

ConsenCUS-D4.2-Selection of temporary storage strategy and description of uncertain parameters or processes-v2-2204

Date	Version	Status	Initials	Changes Marked
28/03/2022	1		NA	
20/06/2022	2		NA	



This project has received funding from the European Union's Horizon 2020 research and Innovation programme under grant agreement N° 101022484.

Version Control Sheet

WP: WP4 CO2 storage

Lead author: Nikolai Andrianov

Contributing Authors: Nikolai Andrianov, Knud Dideriksen, Jolanta Kazmierczak

Due date: 2022-04-30

Date: 2022-06-20

Version: 2

Contact: nia@geus.dk

Dissemination Level: ☒ PU: Public
☐ CO: Confidential, only for members of the consortium
(including the Commission)

Table of contents

Executive summary	4
1 Introduction.....	5
2 Potential CO ₂ storage sites	9
2.1 Stenlille gas storage site	10
2.2 Havnsø structure	13
3 CO ₂ storage modelling	14
3.1 Non-reactive flow modelling	14
3.1.1 Reservoir models.....	14
3.1.2 Thermodynamical model	15
3.1.3 Saturation functions	17
3.1.4 Injection and production constraints	22
3.2 Reactive flow modelling.....	23
3.2.1 Problem formulation	23
3.2.2 Salt precipitation	24
3.2.3 Effect of impurities	27
4 Sensitivity study	34
4.1 Sampling the Brooks-Corey parameters	34
4.2 Impact of saturation functions	36
4.2.1 Stenlille	36
4.2.2 Havnsø	37
4.3 Impact of wells location	39
5 Conclusions.....	43
6 Bibliography	44

Executive summary

One of the objectives of Work Package 4 of the ConsenCUS project is to evaluate the efficiency and safety of temporary and permanent CO₂ storage in saline aquifers by determining the storage capacity and recovery efficiency and estimating the possible injection/production rates with a focus on the role of geochemical interactions between the injected CO₂, the formation water, and the reservoir rocks. The stated objectives will be achieved by first assessing several key uncertainties in reservoir characterization of two geological sites in Denmark, Stenlille and Havnsø. This is the goal of the present deliverable 4.2. In the subsequent work, we will reduce the uncertainties by conducting dedicated laboratory experiments and will include the obtained results into more elaborate modelling studies.

The results of the sensitivity study demonstrate the critical role of rock-fluid interactions and accurate reservoir characterization on the estimates of storage capacity, injectivity, and CO₂ recovery. Reactive flow modelling indicates that there is risk of salt precipitation and acidification from impurities in the CO₂ stream, which can negatively impact reservoir injectivity.

In all considered injection/production scenarios, the efficiency of temporary CO₂ storage does not exceed 30%; achieving this recovery factor is only possible if a large amount of CO₂ is injected in the reservoir for permanent storage (several hundred thousand tons for the considered cases). The duration of this initial CO₂ injection is of the order of years so that the caprock integrity will not be compromised.

Overall, we confirm that both permanent and temporary CO₂ storage is possible in the considered geological structures. The specific operating conditions will be refined once a system modelling framework will be available.

1 Introduction

Carbon dioxide capture, utilization and storage (CCUS) is a crucial greenhouse gas mitigation technology in order to achieve the climate goals (IPCC, 2013), (IPCC, 2022). In particular, CCUS can decarbonize industrial sectors where there is no other low-carbon alternative, such as iron and steel production, cement production, refineries and other chemical industries. Today, *permanent* CO₂ storage in geological formations is considered to be the most mature technology: as of 2021, there are 27 CO₂ storage facilities in operation (Global CCS Institute, 2021). Sleipner, the first commercial storage site in the world, has been continuously operational since 1996 (Cavanagh, 2015). Despite technologies advancement for CCUS in recent years, they remain costly and energy-intensive, and significant developments are needed to drive the economics of CCUS.

One key need is the development of new processes to convert the captured CO₂ into useful commodity materials and chemicals (US DoE, 2017). In the short term, the market for CO₂ use is expected to remain relatively small; in the long term, CO₂ sourced from biomass or the air (i.e. direct capture) could play a key role in a net-zero CO₂ emission economy (IEA, 2019).

Depending on the CO₂ source, the feed-streams vary in terms of both composition and mass flow rate, sometimes substantially. Jensen et al (2014) provide the following estimates:

- The amount of CO₂ produced by a gas- or coal fired power plant depends upon the electricity demand and its variation with time (roughly 78% of the global CO₂ emissions from fossil fuel combustion are attributed to power plants (IPCC, 2005); in Copenhagen, the Avedøre gas-fired power plant alone emits >2 Mt/year). The rates can change by 2% within 45 minutes, and the CO₂ concentrations in the flue gas vary within 10-12%.
- During the operation of a cement plant, CO₂ is produced through the calcination process, by burning fossil fuels to heat the kiln, by producing electricity to operate the machinery, and during transport of the cement product. The cement plants do not run continuously; some plants may only run for a month at a time every few months. The cement industry accounts for approx. 7% of the global CO₂ emissions (IPCC, 2005).
- A CO₂ stream from a petroleum refinery is determined by particular range of crude oil feedstocks and by target products. The CO₂ production per unit volume of processed oil can differ by factor 2. Around 6% of global CO₂ emissions are attributed to refineries (IPCC, 2005).

All the above suggests that CO₂ transportation and storage networks will need to accommodate fluctuations in CO₂ feed-flows. Besides, there are also the following considerations:

- The future low carbon energy systems are anticipated to be dominated by high penetrations of variable renewable energy such as wind and solar (Spitz, 2018). However, renewables are leading to an increased need for grid balancing sources of electricity such as natural gas-fired power plants.
- If CO₂ is shipped for permanent storage, an intermediate buffer storage is needed since shipping occurs in discrete runs while the flow of CO₂ from a source such as a power plant or industrial emitter is continuous. The storage should be sufficient to accommodate unexpected shipping delays so that the CO₂ capture and subsequent liquefaction is not disturbed (BEIS, 2018).
- The food industry and agriculture are consuming certain quantities of CO₂ on the seasonal basis. In the summer period, CO₂ is used to promote crop growth in greenhouses (Koenen, 2018). CO₂ supply for food and beverages preparation is also highest in the summer months (IEA, 2019).
- For decades, CO₂ has been successfully used for enhanced oil recovery (EOR) purposes. Using an offshore aquifer for both CO₂ sequestration and as buffer storage for CO₂-based EOR can potentially increase flexibility and availability of the CO₂ (Kaufmann, Aavatsmark, Nøkleby, & Aurdal, 2016). One of the findings in (Kaufmann, Aavatsmark, Nøkleby, & Aurdal, 2016) is that at retention period of almost three years must incur before back-production can start.

To summarize, there is a need in evaluating different strategies for *temporary* storage of CO₂, which are associated with different time scales:

- Minutes to hours to accommodate fluctuations in CO₂ rates from power plants.
- Days to weeks to ensure smooth shipping for subsequent permanent storage.
- Months for the case of cement plants and refineries.
- Seasonal for the food industry and the agriculture.
- Years for CO₂-based EOR applications.

Various storage options can be considered to address the strategies listed above.

High-frequency CO₂ flow fluctuations can be potentially balanced by linepacking pipelines, i.e., managing the pressure and velocity in the pipeline so that it can be used as an interim storage (Spitz, 2018). Cylindrical storage tanks or floating storage barges can be used to store up to 100,000 tons of liquified CO₂ (BEIS, 2018). Salt caverns can store several hundred thousand tons of CO₂ at supercritical conditions (Dusseault, 2002). All these options have an advantage of high retention rates and provide the same CO₂ purity as in the feed stream. On the downside, the

storage volumes are relatively small. Besides, construction of salt caverns typically takes several years, and the produced water need to be disposed in environmentally responsible way, for example, by pumping it into the sea (Crotagino, 2022).

The objective of the present work is to evaluate the efficiency and safety of temporary and permanent CO₂ storage in saline aquifers by determining the storage capacity and recovery efficiency and estimating the possible injection/production rates with a focus on the role of geochemical interactions between the injected CO₂, the formation water, and the reservoir rocks. To this end, we first assess several key uncertainties in reservoir characterization of two geological sites in Denmark, Stenlille and Havnsø.

An efficient management of a storage site requires an uncertainty assessment for CO₂ storage capacity and injectivity. For the case of temporary storage, we additionally need to evaluate the role of uncertainties in CO₂ production. Some of the crucial questions to ask are:

- What is the range of uncertainty for specific rock and fluid input parameters?
- How does the uncertainty in input parameters propagate to the target characteristics, such as storage capacity, CO₂ injectivity and productivity?
- What can be done to reduce the uncertainty?

Standard methods to quantify this uncertainty rely on considering an ensemble of realizations of a reservoir model and quantifying the statistical measures of the ensemble (Bear & Cheng, 2010). Estimating static capacity is computationally inexpensive. On the other hand, performing dynamic simulations on all realizations can quickly become computationally intractable. Solutions to this problem include either reducing the number of realizations, or simplifying the simulations required for each realization (Allen, Nilsen, Lie, Møyner, & Andersen, 2018).

In the present work, we utilize a relatively coarse reservoir model with a simplified description of fluids in order to get reasonable simulation times for the purpose of uncertainty assessment. In subsequent deliverables, we will reduce the identified critical uncertainties using laboratory experiments and incorporate the results in a more sophisticated reservoir model.

The parameters which influence CO₂ storage modelling can be grouped as follows:

- Static reservoir properties, which define the geometry (horizons, faults) and distribution of rock properties such as porosity and permeability.
- Fluids' properties such as phase density, viscosity, compressibility, chemical composition and components properties.
- Parameters, describing the interaction between the rock and the fluids (relative permeabilities, capillary pressures).

- Gas-fluid-rock geochemical reactions.
- Geomechanical aspects such as rock compaction and fracturing.

All of the above-mentioned parameters can be associated with corresponding uncertainties ranges and the influence of the uncertainty can be examined using sensitivity studies, see e.g. (Manceau & Rohmer, 2016), (Han, Kim, Esser, Park, & McPherson, 2011), (Sarkarfarshi, Malekzadeh, Gracie, & Dusseault, 2014).

In the present work, we study the sensitivity of CO₂ recovery factor with regards to the parameters of the CO₂-water relative permeabilities and capillary pressures, as well as the impact of caprock topology and different well schedules. Subsequent deliverables will address the impact of a refined geological model and detailed geochemical characterization of gas-fluid-rock interactions.

2 Potential CO₂ storage sites

Saline aquifers represent more than 80% of worldwide CO₂ storage capacity; besides, saline aquifers are abundant geographically, which makes it less of a source-sink matching problem than is found in oil and gas reservoirs (Selosse & Ricci, 2017). On the downside, less information is available about storage capacity in saline aquifers as compared to other storage options such as depleted oil and gas fields.

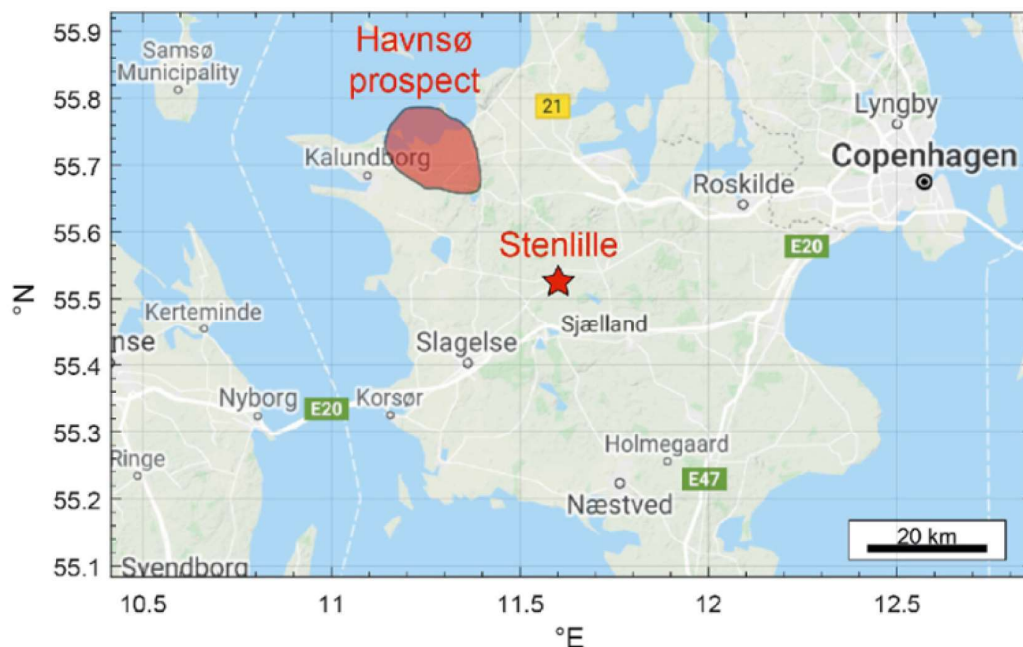


Figure 1. Locations of Stenlille and Havnsø sites (Bredesen, 2022).

The locations of two saline aquifers in the Danish area, considered in this work – Stenlille and Havnsø – are depicted in Figure 1.

The Havnsø structure is considered as one of the most prospective CO₂ storage sites in Denmark, see (Bredesen, 2022) and references therein. The structure is particularly interesting due to the proximity of two large CO₂ emission sources; a biomass-fired power plant and a refinery located close to Kalundborg. In addition, the Danish capital Copenhagen lies only 85 km away with supplementary CO₂ point sources.

However, there is only low-quality seismic data available for Havnsø and no wells have been drilled to evaluate the geological model. Therefore, current assessments of the Havnsø CO₂ prospect are mainly based on extrapolating data from the Stenlille saline aquifer gas storage facility, located approximately 30 km southeast of the Havnsø structure. For details, see (Bredesen, 2022) and the references therein.

2.1 Stenlille gas storage site

The natural gas underground storage is located near the town of Stenlille, approximately 70 km SE of Copenhagen, see Figure 1 and Figure 2. Natural gas has been injected into and stored in the Gassum sandstone reservoir since 1989, serving as a subsurface buffer for the annual supply and demand chain of natural gas.

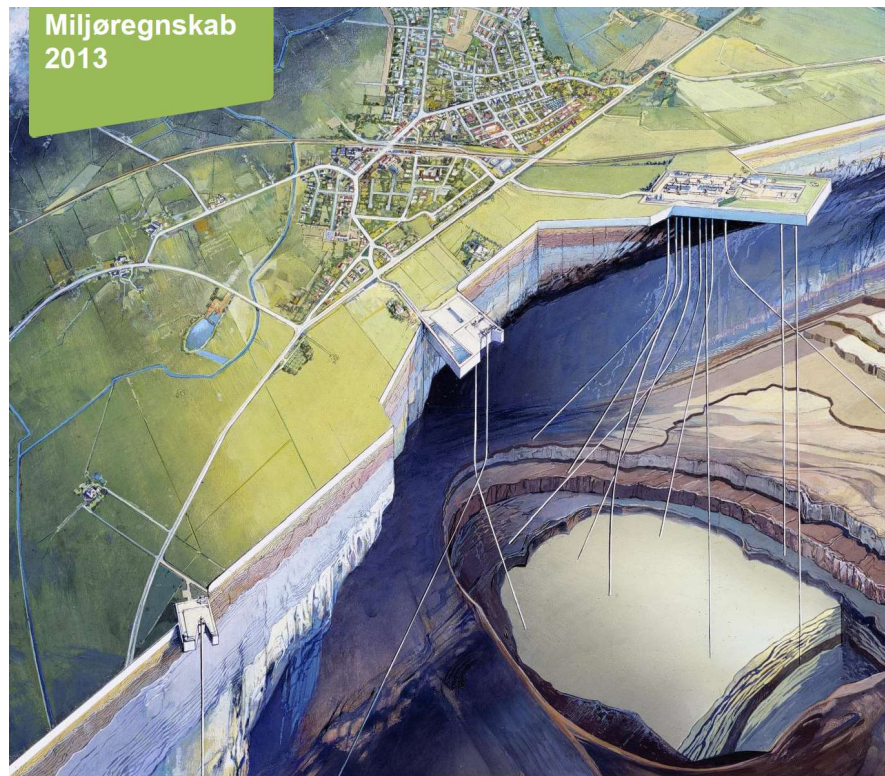


Figure 2. Artistic representation of the Stenlille natural gas underground storage (DONG, 2013).

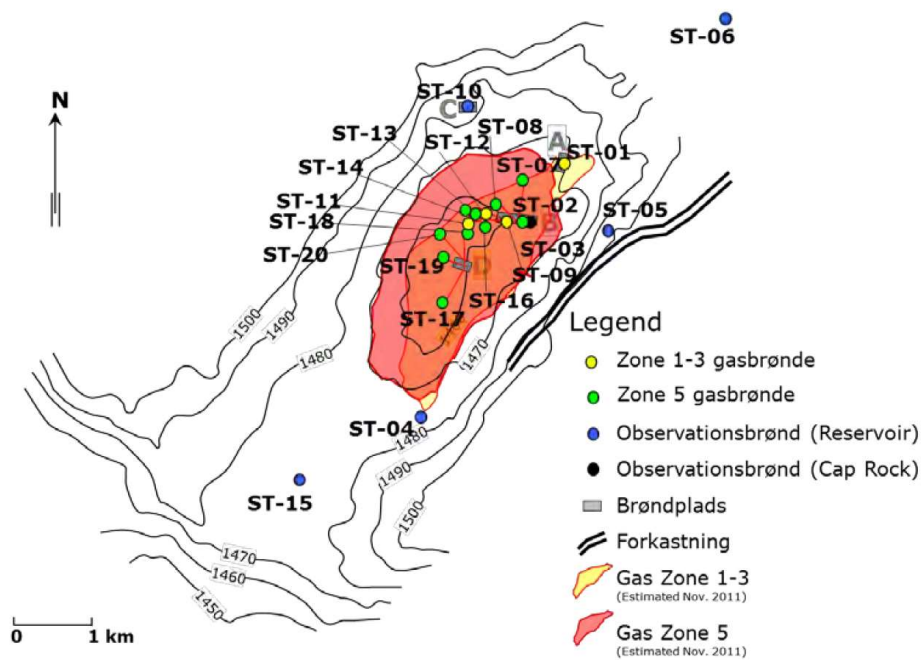


Figure 3. Map view of the Stenlille natural gas underground storage with wells locations (GSD, 2017).

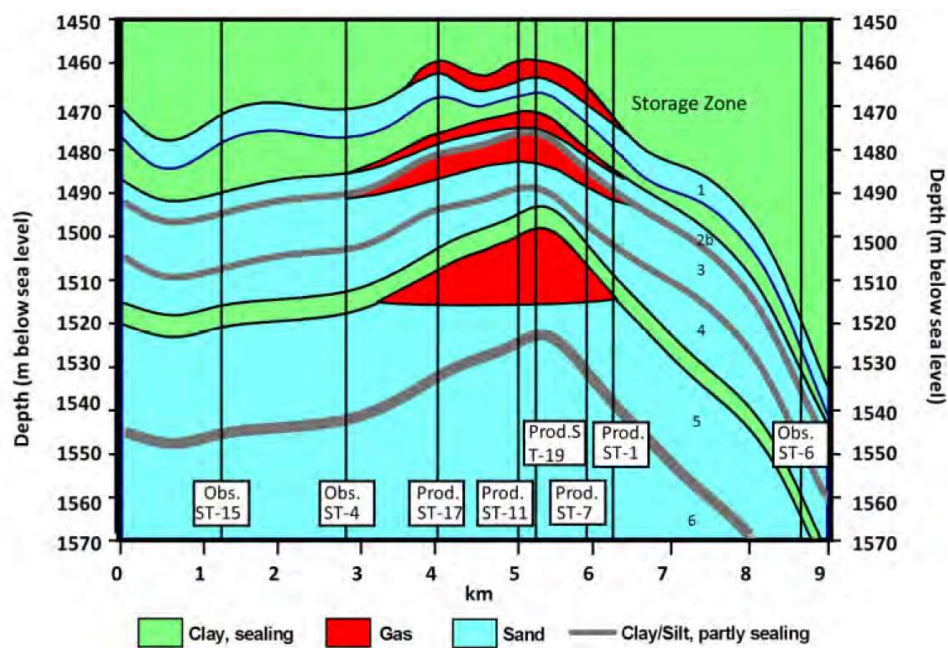


Figure 4. Schematic cross section (SW-NE) of the Stenlille natural gas underground storage including numbering of the different gas zones and well locations (GSD, 2017).

Natural gas is being stored in an anticlinal structure with an expected gas storage capacity of about 1.5 bcm (billion cubic meters at standard conditions) in the upper Triassic Gassum Sandstone Formation 1500–1600 m below the surface; it replaces saline formation water. As of 2017, there are 14 injection and production wells as well as 6 observation wells, see Figure 3.

The reservoir occurs within a domal closure and is overlain by seal-forming mudstones of the Fjerritslev Formation. The geological setting at Stenlille is assumed to represent a good analog to the Havnsø structure since similar lithologies and burial depths for the Gassum Formation are expected. The average porosity (25%) and net-to-gross (0.7) in the Gassum sandstone reservoir at Stenlille represent good conditions for geological CO₂ storage.

The Gassum Sandstone Formation is c. 140 m thick; the upper 40 m of the formation is divided into 5 gas storage zones separated by thin shale beds as indicated in Figure 4. The 300 m thick clay sequence of the Lower Jurassic Fjerritslev Formation above the gas storage reservoir has acted as an efficient seal, since no leakage has been observed (Laier & Øbro, 2009), (GSD, 2017).

The dataset at Stenlille is the most comprehensive onshore dataset in Denmark and has led to a good local understanding of the geological and petrophysical properties of the Gassum sandstone reservoir and the Fjerritslev caprock. The dataset consists of cuttings descriptions, cores, core analysis data, wireline logs, well completions reports, well test reports (Kristensen, 2020), seismic data (Bredesen, 2022), and geochemical data (Holmslykke, Olivarius, Kjøller, & Dideriksen, 2020). Besides, there are historical records of injection and production rates of natural gas, as well as bottomhole and wellhead pressures and temperatures (GSD, 2017). These data have been used to history match the existing Stenlille reservoir model.

Still, there are several limitations with regards to the Stenlille dataset:

- Seismic data contain substantial noise, lack pre-stack seismic gathers and the wells contain sporadic log data content, which constrain methods for quantitative interpretations (Bredesen, 2022). An improved seismic interpretation will address these issues in the subsequent deliverables within ConsenCUS project.
- The data on fluid-rock interaction between CO₂ and the Gassum sandstone rock is limited (Kjøller, et al., 2011), (Weibel, et al., 2011).

The results of sensitivity study in Section 4 will be used to design the experimental studies, needed to improve the predictive power of the reservoir models for Stenlille and Havnsø.

2.2 Havnsø structure

The Havnsø structure covers approximately 160 km² of the Gassum sandstone formation buried at approximately 1500 m depth. One-third and two-thirds of the structure is situated offshore and onshore, respectively, with an estimated storage capacity between 200–400 Mt of CO₂ (Hjelm, et al., 2020).

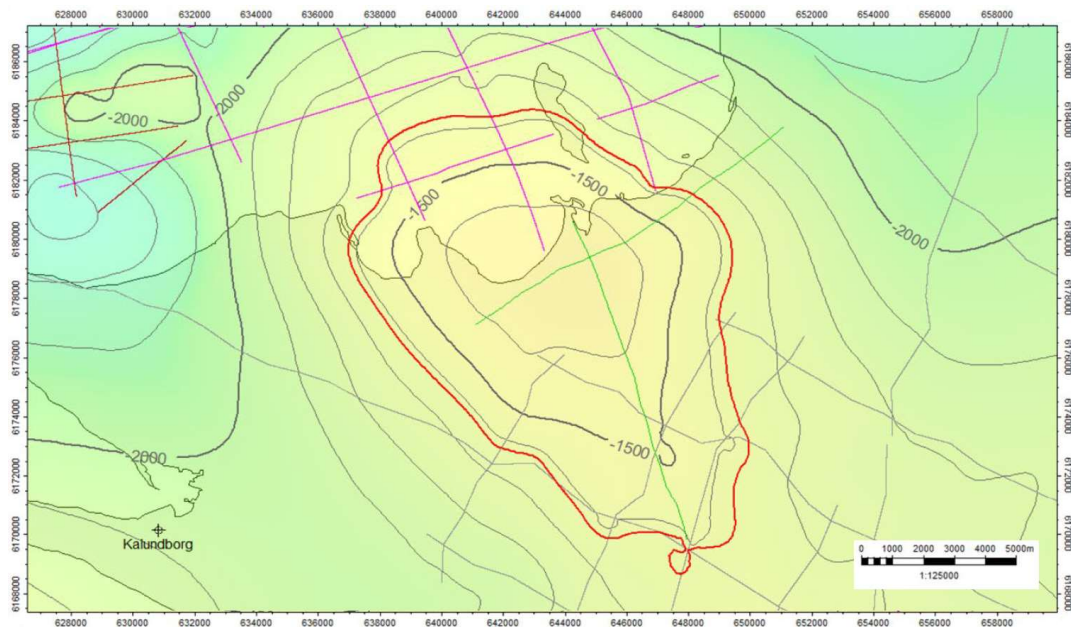


Figure 5. The depth map of the Gassum formation at Havnsø (Hjelm, et al., 2020).

The top surface of Gassum formation at Havnsø is presented in Figure 5. Note that there are uncertainties in the depth map are estimated to be up to 10–15% (or 50–150 m), mainly due to lack of high-resolution seismic data and well data near the two structures (Mathiesen, Laghari, & Rasmussen, 2020).

The distribution of rock properties in the subsurface relies entirely on extrapolation of the preliminary interpretations at Stenlille. Although the overall depositional system is supported by several wells also outside the Stenlille site, the exact pattern of important and influential elements in deposition is very uncertain (Frykman, 2020).

3 CO₂ storage modelling

3.1 Non-reactive flow modelling

In this work, the numerical modelling of CO₂ storage without considering the chemical reactions is done using a commercial reservoir simulator Eclipse 100 (Schlumberger, 2017). A simulation case contains the following information:

- **Reservoir model:** a representation of the reservoir using hexahedral grids, whose geometry is adapted to sedimentary rock bodies and faults. The grid is populated with several properties, such as porosities and permeabilities. Faults and fractures are characterized by prescribing transmissibilities at corresponding grid faces.
- **Thermodynamic model** for the fluids in the reservoir, which provides the corresponding densities, viscosities, compressibilities, and solubilities.
- **Saturation functions:** the relative permeabilities and capillary pressures, which describe the rock-fluid interaction.
- **Well schedule** defines the injection and production wells and their control.

Motivated by certain similarities in depositional environment between the Stenlille and Havnsø structures (Bredesen, 2022), we utilize the same fluid model and the representation of saturation functions in both cases.

3.1.1 Reservoir models

3.1.1.1 Stenlille

In this work, we utilize the structural elements, rock properties, and wells data from the Stenlille reservoir model set up by Hans Øbro (DONG, 2012); see Figure 6.

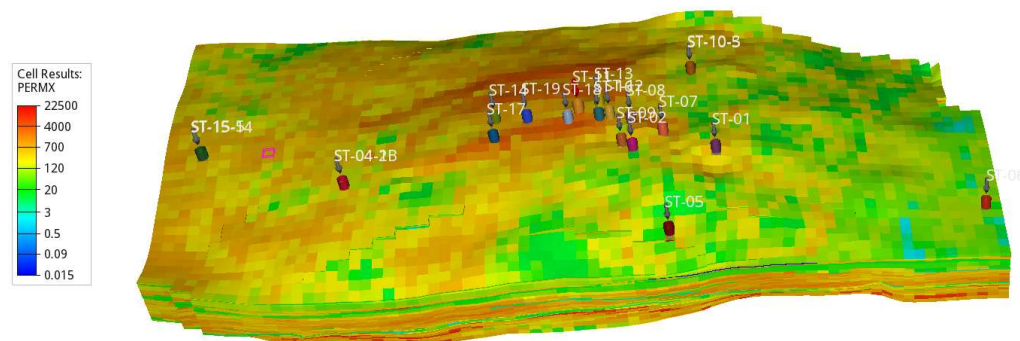


Figure 6. Stenlille wells and the reservoir permeability field.

The model, covering approximately 7,760 x 3,570 x 137 meters, contains 119,634 active cells with properties, adjusted to represent faults and fractures. The reservoir consists of 6 zones, separated by impermeable layers. In total, there are 14 injection/production wells and 6 observation wells. The model is history matched to gas injection/production and pressure data, which makes it a good candidate to model CO₂ injection.

3.1.1.2 Havnsø

The primary input for the reservoir model is the Top Gassum map, obtained from seismic interpretation. A uniform thickness reservoir of approximately 20,000 x 15,000 x 150 m has 4,959,998 active cells. The distribution of rock properties follows the suggested depositional pattern from Stenlille; see (Frykman, 2020) for details.

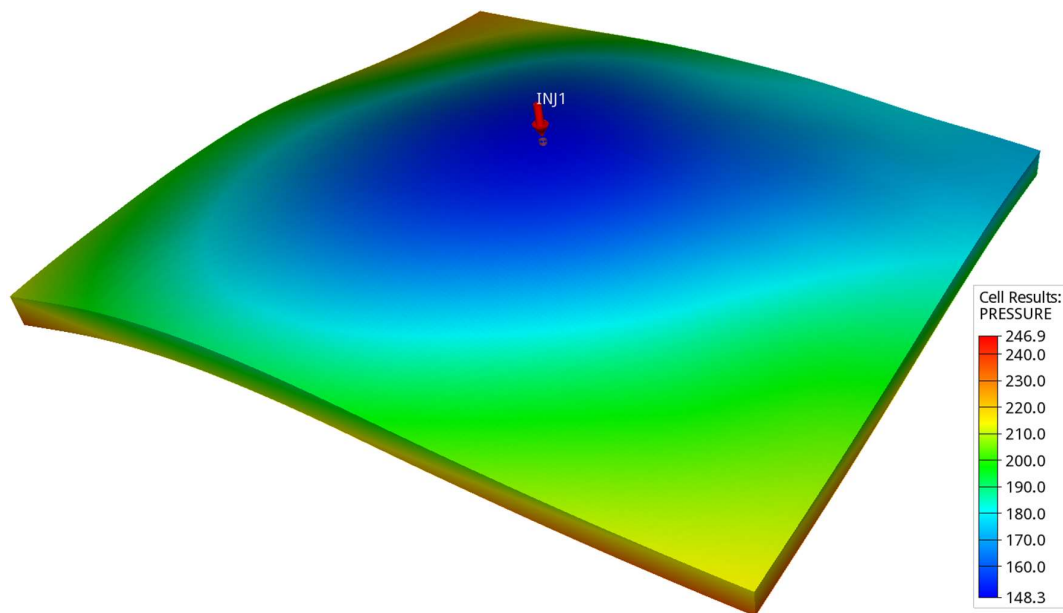


Figure 7. Pressure field for the Havnsø reservoir model and the injection start. A simulation well is in the center of the structure.

3.1.2 Thermodynamical model

The basic concept of CO₂ storage is to use a relatively deep (greater than ~800 m) geological reservoir to ensure that CO₂ is in a dense form – most often as a supercritical phase. This is important for storage efficiency (a higher density means more effective storage) and for storage security as low permeability sealing units are commonly encountered at the depths of around 1 km (Ringrose, 2020).

Injection of high-pressure CO₂ in a geological reservoir is a typical phase-equilibrium problem, which can be solved by application of thermodynamics. If the rocks are unreactive, CO₂ distributes itself between an aqueous liquid phase and CO₂-rich liquid phase, whereas CO₂ solubility depends on pressure, temperature, and phase composition. The problem is much more complicated if dissolution/precipitation of rock-forming minerals occurs. In this case, the rate constants of chemical reactions and the surface areas of minerals must be assessed, and the resulting reactive transport model has to be used (Marini, 2006).

In what follows, we consider a two-phase CO₂-water isothermal model without geochemical reactions.

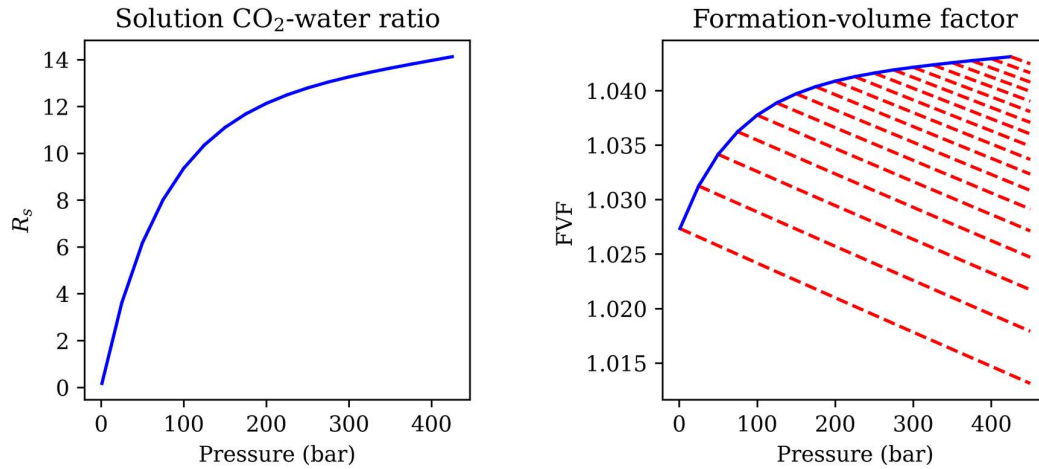


Figure 8. Left: CO₂ solubility. Right: formation volume factor; red lines correspond to a specific solution CO₂-water ratio in the undersaturated brine, blue line corresponds to the brine, saturated with CO₂.

CO₂ dissolution in water (formation brine) is characterized by the solution CO₂-water ratio R_s , i.e., the ratio of the dissolved CO₂ volume per unit volume of water. In the present work, it is assumed that the solution CO₂-water ratio can be approximated by the correlation (Chang, Coats, & Nolen, 1998); the corresponding dependency for a fixed reservoir temperature is presented in Figure 8 (left).

The density of brine with dissolved CO₂ at reservoir conditions ρ_b is linked to the formation-volume factor FVF as follows,

$$\rho_b = \frac{\rho_{bs} + R_s \rho_{gs}}{FVF_b}, \quad (1)$$

where ρ_{bs} is the brine density at surface conditions and ρ_{gs} is the CO₂ density at surface conditions. The dependency of FVF_b as a function of pressure is presented in Figure 8 (right).

For detailed analysis, see (Dake, 1978). In this work, we use the values $\rho_{bs} = 1100 \text{ kg/m}^3$ and $\rho_{gs} = 1.9 \text{ kg/m}^3$.

The effect of dissolved CO_2 on brine viscosity is very small (Chang, Coats, & Nolen, 1998) and has been neglected in this work.

The CO_2 formation volume factor and viscosity are calculated using the correlations of (Bahadori, Vuthaluru, & Mokhatab, 2009) and (Fenghour, Wakeham, & Vesovic, 1998). The corresponding dependencies are presented in Figure 9.

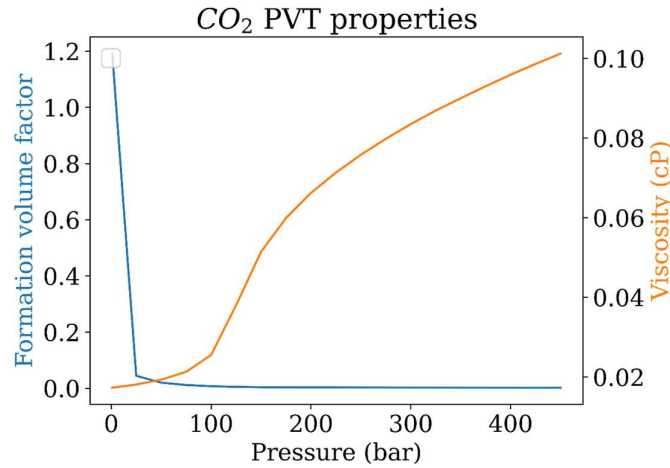


Figure 9. The CO_2 formation volume factor and viscosity as a function of pressure.

The CO_2 density at reservoir conditions ρ_g is linked to the formation-volume factor FVF_g as follows,

$$\rho_g = \frac{\rho_{gs}}{FVF_g}. \quad (2)$$

3.1.3 Saturation functions

3.1.3.1 Basic concepts

When more than one phase is flowing simultaneously through a porous medium, then each fluid has its own effective permeability, which is dependent on the saturations of each fluid (Brooks & Corey, 1964). It has been determined experimentally that the shape of the relative permeabilities and capillary pressures depends on the local saturation history: if the wetting phase is increasing, the functions are referred to as imbibition and drainage otherwise (Dake, 1978).

The water (wetting phase, subscript w) and CO₂ (non-wetting phase, subscript n) flow in the porous medium is described by Darcy's law,

$$\mathbf{u}_\alpha = -\frac{k_{rap}}{\mu_\alpha} \mathbf{K}(\nabla p_\alpha - \rho_\alpha \mathbf{g}), \quad \alpha = w, n, \quad (3)$$

with k_{rap} being the relative permeabilities of phase α during the process $p = d, i$ (drainage or imbibition, respectively), μ_α the viscosity of phase α , \mathbf{K} – the absolute permeability tensor, p_α – the pressure of phase α , ρ_α – the mass density of phase α , and \mathbf{g} – the gravity acceleration.

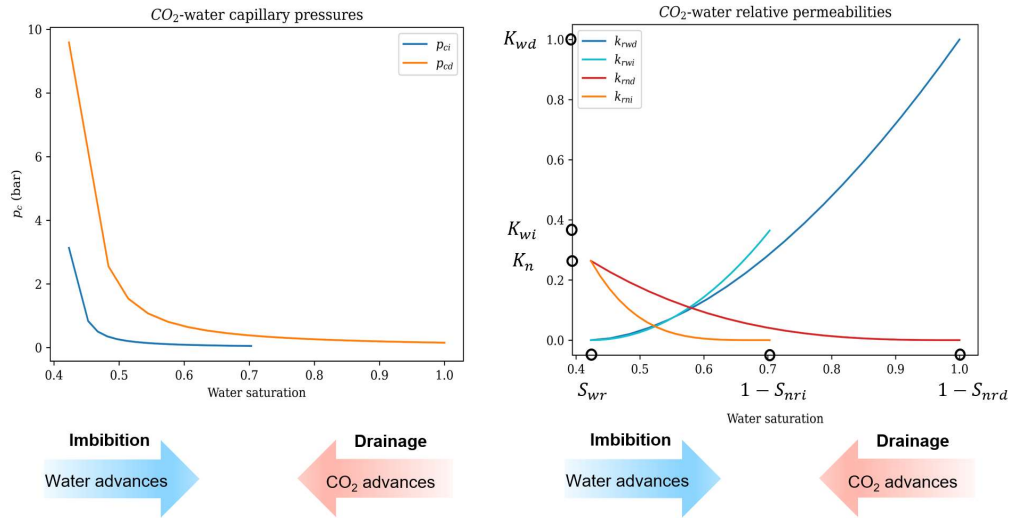


Figure 10. An example of Brooks-Corey CO₂-water drainage and imbibition capillary pressures (left) and relative permeabilities (right).

The phase pressures in (3) are linked via the capillary pressure function, which can be expressed as a function of saturation in the Brooks-Corey form (Brooks & Corey, 1964),

$$p_c = P_e \left(\frac{S_w - S_{wr}}{1 - S_{wr} - S_{nr}} \right)^{-1/\lambda}, \quad (4)$$

where P_e is the entry pressure and λ is a Corey exponent. An example of drainage and imbibition capillary pressures is presented in Figure 10 (left).

The two-phase water-oil relative permeabilities are taken in the Brooks-Corey form:

$$k_{rw} = K_w \left(\frac{S_w - S_{wr}}{1 - S_{wr} - S_{nr}} \right)^{n_w}, \quad k_{rn} = K_n \left(\frac{S_n - S_{nr}}{1 - S_{wr} - S_{nr}} \right)^{n_n}, \quad (5)$$

where S denote the saturations, S_{wr} is the residual water saturation, S_{nr} is the residual CO₂ saturation, n_α is the Brooks-Corey exponent for the phase $\alpha = w, n$, and K are the corresponding endpoint permeabilities.

An example of drainage and imbibition relative permeabilities is presented in Figure 10 (right). As CO₂ is injected in the initially water-filled reservoir, k_{rnd} (red line in Figure 10) gradually increases and k_{rwd} (blue line) decreases until the critical water saturation S_{wr} is reached. Water saturation S_w cannot decrease any further because by (3) $k_{rwd}(S_{wr}) = 0$. During CO₂ migration or production S_w increases, but the CO₂ relative permeability now follows the imbibition branch k_{rwd} (yellow line). Experimental data demonstrate that $1 - S_{nri} < 1 - S_{nrd}$, which means that the corresponding difference in injected CO₂ remains in the reservoir. This phenomenon is termed capillary trapping, which is one of the essential CO₂ trapping mechanisms (IPCC, 2005), (Juanes, Spiteri, Orr, & Blunt, 2006).

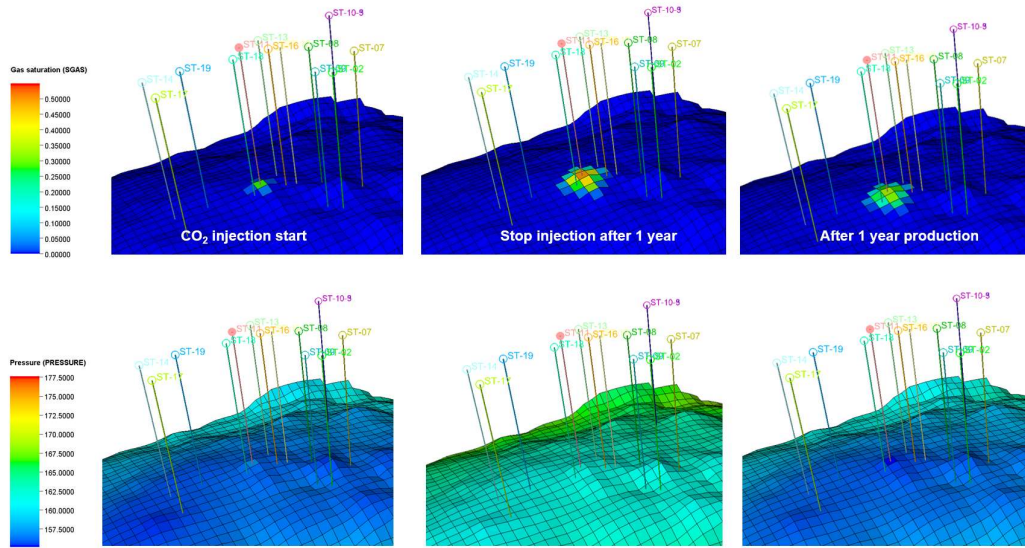


Figure 11. Example of reservoir-scale effects of capillary trapping of injected CO₂.

In terms of the temporary CO₂ storage, capillary trapping contributes to a lower CO₂ recovery factor as illustrated in Figure 11. The top row in Figure 11 demonstrates the evolution of CO₂ saturation, and the bottom row – the corresponding pressure field during a 1-year CO₂ injection of approximately 100,000 tons/year in the top zone of the water-filled Stenlille reservoir model, followed by a 1-year CO₂ production using a minimal tubing head pressure control. The trapped gas after the production stop is visible in the top-right plot in Figure 11.

3.1.3.2 Experimental data

It has been long recognized that accurate measurement of relative permeabilities and capillary pressures is important for reliable estimates of CO₂ storage capacity, well injectivity, extent of capillary trapping, and leakage through the seal (Benson, Pini, Reynolds, & Krevor, 2013). Despite that fact that many experimental studies have been reported in the literature, there are

relatively few which provide tabular core flooding data on the drainage and imbibition branches of relative permeabilities and capillary pressures for CO₂-brine systems using various rock types.

In this work, we have used the relative permeability datasets from (Bennion & Bachu, 2005), (Bennion & Bachu, 2006), (Akbarabadi & Piri, 2013). The experimental data points are presented in Figure 12. The wide scatter of the data is partly due to the varied lithologies analyzed; note that not all lithologies are represented in the reservoirs, considered in this report. Still, the presented data indicate the range of variability of the rock curves for the CO₂-brine systems.

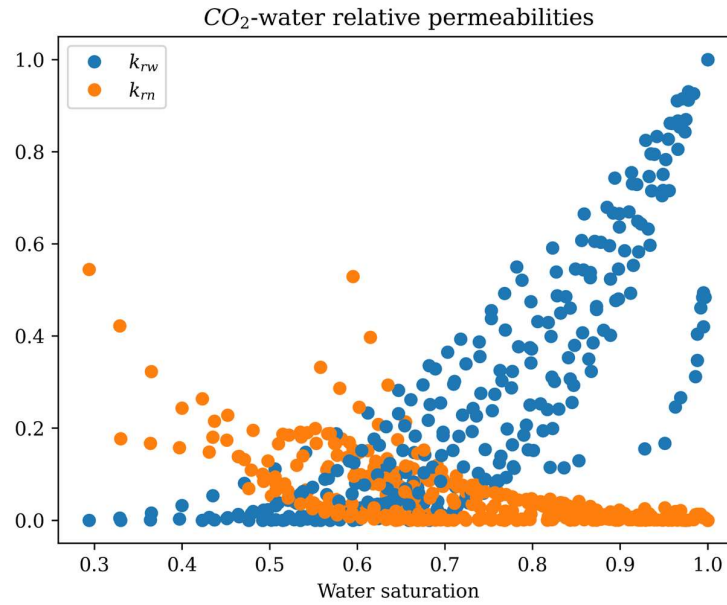


Figure 12. Experimental data on relative permeabilities by (Bennion & Bachu, 2005), (Bennion & Bachu, 2006), (Akbarabadi & Piri, 2013).

The experimental data were fitted using the Brooks-Corey form (5); the best fits for the Brooks-Corey parameters S_{wr} , S_{nr} , K_w , K_n , n_w , n_n are presented in Table 1.

Table 1. Best fits for experimental data using the Brooks-Corey parametrization.

Experimental data	Type	S_{wr}	S_{nr}	K_w	K_n	n_w	n_n
(Akbarabadi & Piri, 2013); Exp24	drain	0.52	0	1	0.19	52.71	1.70
(Akbarabadi & Piri, 2013); Exp24	imb	0.52	0.36	0.09	0.19	5.42	0.59
(Akbarabadi & Piri, 2013); Exp25	drain	0.54	0	1	0.19	47.49	1.57
(Akbarabadi & Piri, 2013); Exp25	imb	0.54	0.33	0.07	0.19	1.79	0.48
(Bennion & Bachu, 2005); Basal	drain	0.29	0	1	0.54	1.83	4.93

(Bennion & Bachu, 2005); Cooking	drain	0.48	0	1	0.07	3.31	5.12
(Bennion & Bachu, 2005); Ellerslie	drain	0.66	0.03	0.80	0.12	2.05	1.91
(Bennion & Bachu, 2005); Nisku	drain	0.33	0	1	0.18	2.77	1.10
(Bennion & Bachu, 2005); Viking	drain	0.56	0.04	0.72	0.33	3.14	2.50
(Bennion & Bachu, 2005); Wabamun	drain	0.57	0	1	0.19	1.41	2.10
(Bennion & Bachu, 2005); Wabamun, High K	drain	0.55	0	1	0.20	1.80	3.44
(Bennion & Bachu, 2005); Wabamun, Low T	drain	0.68	0	1	0.09	1.50	1.47
(Bennion & Bachu, 2005); Wabamun, Low K	drain	0.60	0.04	0.86	0.53	1.42	4.95
(Bennion & Bachu, 2006); Nisku	drain	0.49	0	1	0.10	2.71	4.54
(Bennion & Bachu, 2006); Nisku	imb	0.49	0.22	0.55	0.10	2.16	4.28
(Bennion & Bachu, 2006); Viking	drain	0.42	0	1	0.26	1.73	2.84
(Bennion & Bachu, 2006); Viking	imb	0.42	0.30	0.36	0.26	2.04	3.94

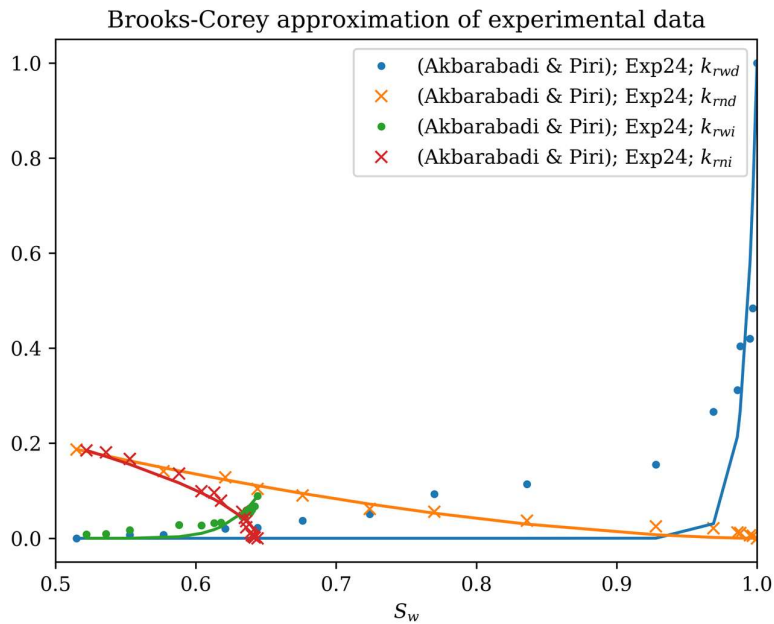


Figure 13. Brooks-Corey approximation of the drainage and imbibition relative permeabilities from experiment 24 in (Akbarabadi & Piri, 2013).

Not all experimental data can be accurately represented using the Brooks-Corey parametrization as can be seen in Figure 13. In particular, the Brooks-Corey parametrization cannot accurately reproduce the drainage branch of the water relative permeability. Still, we argue that the Brooks-Corey parametrization is suitable to merely identify the ranges of the parameters S_{wr} , S_{nr} , K_w , K_n , n_w , n_n for drainage and imbibition, see Table 2.

Table 2. Brooks-Corey parameter ranges for relative permeabilities.

Range	S_{wr}	S_{nrd}	S_{nri}	K_{wd}	K_{wi}	K_n	n_{wd}	n_{wi}	n_{nd}	n_{ni}
min	0.29	0	0.2	0.7	0.05	0.05	1.4	1.7	0.47	0.4
max	0.67	0.05	0.36	1	0.55	0.55	53	5.5	5.2	4.3

Since there is significantly less data on the drainage and imbibition capillary pressures compared to the relative permeability data, we consider the approximate parameter ranges from the literature (Pini, Krevor, & Benson, 2012), (Jackson & Krevor, 2020); see Table 3. Note that the entry pressures P_e and the exponents λ for the drainage branch are larger than their imbibition counterparts (Dake, 1978).

Table 3. Brooks-Corey parameter ranges for capillary pressures.

Range	P_{ei} (bar)	$P_{ed}-P_{ei}$ (bar)	λ_i	$\lambda_d - \lambda_i$
min	8E-03	0	0.5	0
max	5E-02	1E-02	0.8	0.15

3.1.4 Injection and production constraints

Kaufmann et al. (2016) identify the following constraints, related to CO₂ injection in saline aquifers and its back-production:

1. Tubing head pressure constraint to keep the produced CO₂ in supercritical state.
2. Limited water content in produced CO₂ to avoid hydrates and wellbore corrosion.
3. Limited injection pressure to avoid rock failures.

In this work, we limit ourselves to the constraint #3; other constraints will be addressed in subsequent deliverables.

The question whether an injection pressure will exceed the fracturing pressure is one of the subjects of reservoir geomechanics (Zoback, 2007). A comprehensive answer to this question requires building a geomechanical model, which is based on the knowledge of the rock mechanical properties and state of stresses in the reservoir.

Since a detailed geomechanical modelling lies out of the scope of the current project, in this work we use an empirical approach to estimate the fracturing pressure. Following Wangen (2002), we assume that the fracturing pressure is 75% of the lithostatic pressure.

For Stenlille wells, the average true vertical depth of well completions is approximately 1520 m. Well logs data (Kristensen, 2020) suggest that the average rock density in the reservoir and in the overburden can be estimated as 2300 kg/m³. With these estimates, the lithostatic pressure is approximately 342 bar, and the fracturing pressure is 257 bar. In the Stenlille simulations in Section 4, we use this value as a bottomhole pressure to control the CO₂ injection.

For Havnsø, the top completion of the only well is at 1455 m with initial pressure of 157 bar. The lithostatic pressure is 328 bar, and the fracturing pressure can be estimated as 246 bar. In the Havnsø simulations in Section 4, the fracturing pressure is used to control the CO₂ injection, and the initial pressure – the CO₂ production.

3.2 Reactive flow modelling

In this work, the reactive transport modelling was performed using TOUGHREACT v3.32 (Xu, et al., 2011), (Xu, Sonnenthal, Spycher, & Zheng, 2017). The ECO2N module was used for description of CO₂ and brine properties (Pruess, 2005). Additional geochemical calculations were done with PHREEQC v3 (Parkhurst & Appelo, 2013).

3.2.1 Problem formulation

Consider a two-dimensional (2D) radial model with 20 cells with the height of 3.5 m for the top 8 cells, 7 m for the next 8 cells and 14 m for the bottom 4 cells and 56 cells with increasing width from 0.25 m at the injection point to approx. 30 km for the outermost cell.

The saturation functions were taken in van Genuchten-Mualem (van Genuchten, 1980), (Mualem, 1976) form, i.e.,

$$k_{rw} = \left(\frac{S_w - S_{wr}}{1 - S_{wr}} \right)^{1/2} \left(1 - \left(1 - \left(\frac{S_w - S_{wr}}{1 - S_{wr}} \right)^{1/\lambda} \right)^\lambda \right)^2, \quad (6)$$

$$k_{rn} = \left(1 - \frac{S_w - S_{wr}}{1 - S_{wr} - S_{nr}} \right)^2 \left(1 - \left(\frac{S_w - S_{wr}}{1 - S_{wr} - S_{nr}} \right)^\lambda \right), \quad (7)$$

$$p_c = -P_0 \left(\left(\frac{S_w - S_{wr}}{1 - S_{wr} - S_{nr}} \right)^{-1/\lambda} - 1 \right)^{1-\lambda}, \text{ with } p_c > -p_{c,\max}. \quad (8)$$

The specific values for the parameters of the simulation set up are presented in Table 4. In the parameterization of the capillary pressure, S_{wr} was set to a slightly lower value of 0.25, as recommended in the software documentation.

In what follows, we study the geochemical effects of CO₂ injection with a constant rate in the top 4 cells of the center of the radial mode.

Table 4. Parameters for the 2D reactive flow model.

Parameter	Value
Porosity	0.245
Horizontal permeability	588 mD
Vertical permeability	58.8 mD
λ	0.457
S_{wr}	0.3
S_{nr}	0.05
P_0	0.02 bar
$p_{c,max}$	2 bar

The composition of Stenlille brine is presented in Table 5. Note that brine is highly saline, dominated by close to 3 moles/kg water for Na^+ and Cl^- . In addition, it contains a substantial amount of Ca^{2+}

Table 5. Formation water composition used in calculations (moles per kg water).

Parameter	Value
pH	6.3
Na^+	2.52
HCO_3^-	$1.26 \cdot 10^{-3}$
SO_4^{2-}	$1.56 \cdot 10^{-4}$
Cl^-	3.05
Fe^{2+}	$1.07 \cdot 10^{-3}$
SiO_2	$2.66 \cdot 10^{-4}$
Ca^{2+}	0.2
Mg^{2+}	$6.75 \cdot 10^{-2}$
K^+	$9.46 \cdot 10^{-3}$

3.2.2 Salt precipitation

Since CO_2 contains only about 100 ppm of water, water will transfer from brine to the supercritical CO_2 . This evaporation will increase the concentration of dissolved ions; this will eventually lead to concentrations exceeding the solubility of salts, causing them to precipitate. If such precipitation occurs only in smaller amounts, it will have negligible effect on porosity and permeability. However, the cyclic injections and productions are expected to provide alternating input of dry

gas and salty brine to the near-well environment. If so, much more extensive precipitation could occur with potential significant implications on flow patterns. The experimental and numerical studies of salt precipitation during CO₂ injection are presented in (Pruess, 2009), (Ott, Roels, & De Kloe, 2015), (Peysson, 2014), (Miri & Hellevang, 2016).

The modelling below is performed with the ECO2N module only, meaning that geochemical reactions other than CO₂ dissolution, H₂O evaporation and salt precipitation were omitted. The included reactions were assumed to occur instantaneously so that equilibrium was established at all times. The module only considers NaCl in its treatment of salt precipitation. Na⁺ and Cl⁻ are the major ions of the Gassum brine. However, Ca²⁺ also occurs in substantial concentration and the effect of this ion was not included, conferring some uncertainties to the calculations.

Figure 14 shows the spatial distribution of CO₂ saturation after 10 years of CO₂ injection at 0.1 Mt CO₂ per year. For all simulations, supercritical CO₂ propagates approximately 700 m from the injection well and occupies predominantly the top ~25 meters of the reservoir.

Tests of selected calculations with 4 times larger lateral cell density for the first 1000 m yielded practically the same results, indicating that the cell dimensions used capture the essential aspects in the simulations. Changing the values of certain other parameters affect this distribution somewhat, though. A different choice of S_{wr} and S_{nr} from the base set within the range given in Table 1 provides for deeper, but less laterally extensive CO₂ plume distribution. All simulations predict the formation of halite, but for most simulations the amount is modest. Notably, the salt distribution is predicted to depend on vertical permeability and injection rate (resulting in same total injection amount). Thus, the maximum fraction of the pore space with halite increases with increasing vertical permeability and with decreasing injection rate. Such condition would favor influx of brine from differences in capillary pressure into zones with flow of anhydrous CO₂. Qualitatively, these results fall within with the general finding reported for TOUGH-based modelling (e.g., Pruess (2009)), although substantial uncertainties surround the modelled results because a generally accepted scientific approach to describe the salient processes has not been developed (Miri & Hellevang, 2016).

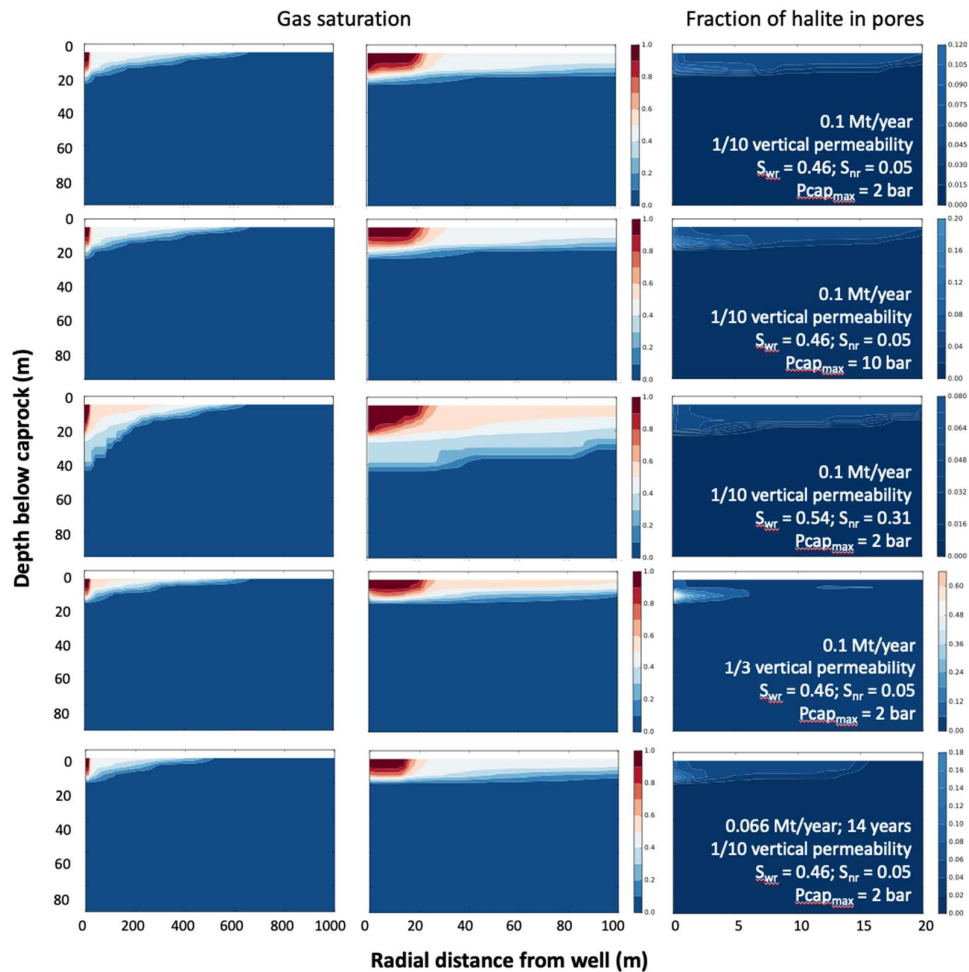


Figure 14. Left column: spatial distribution of CO₂ saturation after injection of 0.1 Mt CO₂ per year for 10 years. Middle column: zoom of the left column. Right column: halite fraction in pores. The rows correspond to different simulation parameters, listed in the right column. The contour map was constructed using linear interpolation between points.

The results indicate that injection of 1 Mt of CO₂ over 10 years would not result in notable salt precipitation although salinity is high in the formation water. Given that salt formation to some degree is linked to the vertical permeability, we would expect that the division of the Stenlille reservoir in zones separated by layers of lower permeability would limit the maximum fraction of pore space that would become filled with halite. Moreover, if salt precipitates to more readily beneath the injection level, as most clearly seen for the scenario with higher vertical permeability, this could decrease the influx of brine to the injection point and limit salt formation at this critical location.

Accurately predicting the decrease in permeability that salt precipitation could give rise to is complicated, however, because it depends on the location in the pore space where it precipitates. Typically, solids nucleate on interfaces (heterogeneous nucleation) because of favorable surface free energies or because of increased fluxes. Thus, it is quite feasible that nucleation and growth may occur in pore throats because of favorable heterogeneous nucleation kinetics. Alternatively, it could form at the water/CO₂ meniscus from which it could be transported to pore throats. Whether the particles become trapped here would depend on a range of factors, including the particle or aggregate size. Thus, although the fractional abundance of salt precipitation in the pore space is relatively modest for most modelled parameter sets, we cannot exclude that salt formation could pose a problem for maintained injectivity.

3.2.3 Effect of impurities

3.2.3.1 CO₂ composition

After capture, the main component by far is CO₂. However, it will contain a variety of impurities with a concentration depending on source, capture technique and processes downstream in the transport chain (Rütters, et al., 2022). Because the capture and transport capabilities are not yet in place, the exact composition of the CO₂ stream is currently unknown. Moreover, CO₂ streams from several sources would most likely be transported, the relative volume of which is not yet given. Consequently, much uncertainty exists about the composition of the injected CO₂ and its temporal variability. Several studies have been performed to assess the identity of the impurities and their likely maximum concentration (Talman, 2015), (Rütters, et al., 2022). In addition, CCS projects in development have defined CO₂ specifications.

Three examples of the maximum proposed CO₂ compositions are given in Table 6, listing only the constituents of likely importance to geochemical reactions. For the Northern Lights and Porthos project, the compositions do not consider gas incompatibility, whereas Rütters et al. (2022) provide values for two types of compatible gasses. Of the three, the most thoroughly evaluated CO₂ composition stems from the cluster analysis by Rütters et al. (2022). Based on the assumption that CO₂ would be mainly captured at sources with an oxidizing composition and that negligible loss would occur during transport, we have based our simulations on an impurity concentration of 6700 mole ppm for O₂, 70 for SO_x and 110 for NO_x, values that are slightly higher for SO_x and NO_x than those assumed for the Northern Lights and Porthos projects and much higher for O₂.

Table 6. Examples of the maximum concentrations of constituents of clear geochemical importance (mol based ppm) for injected CO₂.

Origin	Northern Lights	Porthos	Rütters et al., 2022	
Type	-	.	Reducing	Oxidizing
H ₂ O	30	70	50	50
O ₂	10	40		6700
SO _x	10	20*		70
NO _x	10	5		110
H ₂ S	9	5*	50	
Ammonia	10	3		

* Subject to total sulphur compounds being less than 20 ppm

3.2.3.2 NO_x, SO_x and O₂ reactions

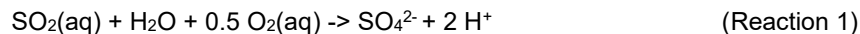
The oxidizing impurities can undergo a range of reactions that involves the impurities themselves, constituents of the formation, and water. In addition, the reactions can be catalyzed by dissolved metals and presumably by the presence of solid phases, similar to what is seen for reactions between O₂ and Fe(II). This greatly complicates the calculations.

The reactive transport model was set up for co-injection of CO₂ into the Gassum Formation with an oxidizing mixture of impurities that consisted of gaseous O₂, SO₂ and NO₂ (henceforth denoted with the subscript "(g)"). Dissolution of gaseous species in water is a fast process and was therefore modeled as an equilibrium reaction. *TherAkin10.dat* database was developed by introducing solubilities of O₂(g) and SO₂(g), taken from Shock et al. (1989), and the solubility of NO₂(g) derived from (Squadrito & Postlethwait, 2009). Log₁₀ was calculated for Henry's constants (K_H in mol atm⁻¹ L⁻¹) of O₂(g), SO₂(g) and NO₂(g) at 0, 25, 60, 100, 150, 200, 250 and 300°C. Values of log₁₀K_H are summarized in Table 7.

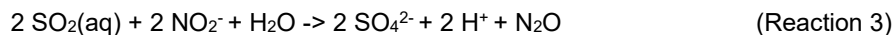
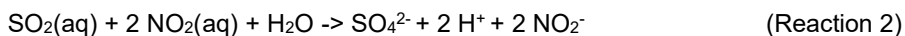
Table 7. Log₁₀K_H for oxidizing impurities derived from Shock et al. (1989) for O₂(g) and SO₂(g) and from (Squadrito & Postlethwait, 2009) for NO₂(g).

Reaction	Log ₁₀ K _H							
	0°C	25°C	60°C	100°C	150°C	200°C	250°C	300°C
O ₂ (g) -> O ₂ (aq)	-2.6570	-2.8980	-3.0630	-3.1080	-3.0350	-2.8740	-2.6490	-2.3540
SO ₂ (g) -> SO ₂ (aq)	0.6527	0.2406	-0.2594	-0.6088	-0.8536	-0.9728	-1.0084	-0.9623
NO ₂ (g) -> NO ₂ (aq)	-1.5929	-1.9136	-2.2817	-2.6179	-2.9487	-3.2096	-3.4206	-3.5948

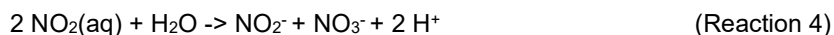
The impurities present in the oxidizing mixture react with each other and water. The major reactions identified in the system are summarized below. $\text{SO}_2(\text{aq})$ is oxidized by $\text{O}_2(\text{aq})$ according to the reaction (Möller, 1988):



Alternatively, $\text{SO}_2(\text{aq})$ may be oxidized by $\text{NO}_2(\text{aq})$ and NO_2^- (Wang, et al., 2020):



$\text{NO}_2(\text{aq})$ interacts also with water resulting in decomposition of nitrous acid (Park & Lee, 1988):



Reactions 1–4 were introduced into the model as kinetically controlled. Rate of sulfate formation according to Reaction 1 depends on the $\text{SO}_2(\text{aq})$ concentration and at pH = 5 is described with a rate expression:

$$d[\text{SO}_4^{2-}]/dt = k_1[\text{SO}_2(\text{aq})],$$

with $k_1 = 2.7 \times 10^{-6} \text{ mol L}^{-1} \text{ s}^{-1}$ (Möller, 1988). Rate of sulfate formation with Reaction 2 depends on the concentration of $\text{SO}_2(\text{aq})$ and $\text{NO}_2(\text{aq})$. For the pH range 5.3–6.8 the rate expression is given as:

$$d[\text{SO}_4^{2-}]/dt = k_2[\text{NO}_2(\text{aq})][\text{SO}_2(\text{aq})],$$

with $k_2 = 1.24 \times 10^7 \text{ mol L}^{-1} \text{ s}^{-1}$ (Wang, et al., 2020). Oxidation of $\text{SO}_2(\text{aq})$ by NO_2^- depends on the concentration of $\text{SO}_2(\text{aq})$, NO_2^- and pH, and at pH <4 the rate expression for Reaction 3 is:

$$d[\text{SO}_4^{2-}]/dt = k_3[\text{H}^+]^{0.5}[\text{NO}_2^-][\text{SO}_2(\text{aq})],$$

where $k_3 = 142 \text{ mol}^{-3/2} \text{ L}^{-1} \text{ s}^{-1}$ (Wang, et al., 2020). Decomposition of nitrous acid depends on the $\text{NO}_2(\text{aq})$ concentration and is described by the rate expression:

$$d[\text{NO}_2^-]/dt = k_4[\text{NO}_2(\text{aq})]^2,$$

with $k_4 = 8.4 \times 10^7 \text{ mol L}^{-1} \text{ s}^{-1}$ (Park & Lee, 1988). Reaction rates and power terms for Reactions 1–4 are summarized in Table 8. To prevent activities of reactants from becoming exceedingly small, the reactions were given an arbitrary equilibrium constant, K and the reaction rate was set to decrease upon approach to equilibrium with a rate modification of $(1-Q/K)$, where Q represent the activity product. Based on the lack of convergence in calculations, log K was set between 35 and 50, which was sufficient to guarantee essentially complete reaction. Finally, rates for the oxidation of Fe(II)aq by O_2 was included based on the homogenous oxidation rates given by

Millero et al. (1987). The rate constant was calculated assuming that the pH dependence is constant at lower pH (the ~4.5 occurring during CO₂ injection), based on findings at lower temperature (e.g., Morgan and Lahav, 2007).

Table 8. Reaction rates and power terms for interactions between oxidizing mixture of impurities and water.

Reaction	Rate [mol L ⁻¹ s ⁻¹]	Power terms		
SO ₂ (aq) + H ₂ O + 0.5 O ₂ (aq) -> SO ₄ ²⁻ + 2 H ⁺	2.7 × 10 ⁻⁶	[SO ₂ (aq)] ¹		
SO ₂ (aq) + 2 NO ₂ (aq) + H ₂ O -> SO ₄ ²⁻ + 2 H ⁺ + 2 NO ₂ ⁻	1.24 × 10 ⁷	[NO ₂ (aq)] ¹	[SO ₂ (aq)] ¹	
2 SO ₂ (aq) + 2 NO ₂ ⁻ + H ₂ O -> 2 SO ₄ ²⁻ + 2 H ⁺ + N ₂ O	142	[H ⁺] ^{0.5}	[NO ₂] ¹	[SO ₂ (aq)] ¹
2 NO ₂ (aq) + H ₂ O -> NO ₂ ⁻ + NO ₃ ⁻ + 2 H ⁺	8.4 × 10 ⁷	[NO ₂ (aq)] ²		
Fe ²⁺ + H ⁺ 0.25 O ₂ -> Fe ³⁺ + 0.5 H ₂ O	2.4 × 10 ⁻⁵	[Fe ²⁺]	[O ₂]	

In addition to the impurities' reaction, the most reactive of the solids in the formation were also allowed to dissolve and/or precipitate if they became supersaturated. Finally, diaspore, hematite, anhydrite and amorphous silica were allowed to precipitate to provide a sink for Al, Fe and Si released from dissolution. The degree of equilibration for a given mineral was given as the saturation ratio, Ω , between the ion activity product (IAP) and the solubility product (Ksp) of the phase. For a mineral AB dissolving to produce A^{x+} and B^{y-}, for example, Ω is:

$$\Omega = \frac{IAP}{Ksp},$$

where:

$$IAP = (A^{x+})_{ac}(B^{y-})_{ac},$$

and:

$$Ksp = (A^{x+})_{eq}(B^{y-})_{eq}.$$

The rate of mineral dissolution was expressed as:

$$r_+ = A_a e^{\frac{-E_{a(a)}}{R} \frac{1}{T}} (X^+)^n + A_n e^{\frac{-E_{a(n)}}{R} \frac{1}{T}}.$$

Here, r_+ is the surface normalized dissolution rate at far from equilibrium for a given mineral (mol/m²/s); A_a and A_n are preexponential factors for the reactions at acidic and the neutral conditions (mol/m²/s), E_{a(a)} and E_{a(n)}, the corresponding activation energies of the reactions (kJ/mol); R is the gas constant (8.314×10⁻³ kJ/mol/K); T, the absolute temperature (K). (X⁺)

represents the activity of a substance influencing the dissolution rate; and n, the reaction order with respect to the activity of the substance.

As dissolution reactions progress, the solution become increasingly saturated with respect to the dissolving minerals, which slow dissolution rates. To account for this, the net dissolution rate per surface area (r_{net}) was calculated by:

$$r_{net} = r_+ (1 - \Omega).$$

The parameters used in the calculation of the rock-water interaction are given in Table 9, with values for the parameters for kinetically controlled reactions taken from (Palandri & Kharaka, 2004).

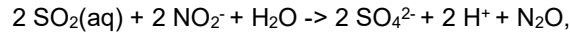
Table 9. Reaction conditions and parameter for mineral dissolution and precipitation.

	Calcite	Siderite	Diaspore	Hematite	Anhydrite	SiO ₂ (a)	Oligoclase	K-Feldspar
Formula	CaCO ₃	FeCO ₃	AlOOH	Fe ₂ O ₃		SiO ₂	Na _{0.8} Ca _{0.2} Al _{1.2} Si _{2.8} O ₈	KAlSi ₃ O ₈
Abundance (vol%)	1%	1%	0%	0%	0%	0%	1%	3%
Log Ksp (25°C)	1.854	-0.187	-15.292	0.109	-4.297	-2.720	-97.779	-22.910
Reaction type	Equilibrium						Kinetic	Kinetic
A_a							10 ^{-9.67}	10 ^{-10.06}
A_n							10 ^{-11.84}	10 ^{-12.41}
E_{a(a)}							65	51.7
E_{a(n)}							69.8	38.0
n							0.457	0.5

Two types of calculations were performed, one where rock-water interaction was omitted and one where it was included. Calculations without rock water interaction predicts that quite low pH will occur in the vicinity of the well, about pH of 1 (Figure 15, first row, first column). Note that dry cells are featured with a pH of 0. Their distribution is visible as dark blue regions in the Figure for pH in the second row. For other species in dry cells, concentration is given in moles per liter medium. For this simulation, the acidification results in the buildup of SO₄²⁻ and NO₃⁻ at the boundary

between very high gas saturation and mixed saturation. On the other hand, NO_2^- only exists at low concentration.

When rocks are present, the concentrations of SO_4^{2-} and NO_2^- are markedly shifted, so that NO_2^- increases at the expense of SO_4^{2-} . This change in the impurities' reaction pathway reflects the pH dependence of the reaction:



which at lower pH consumes NO_2^- and produces SO_4^{2-} . In addition, some of the produced sulphate precipitates as anhydrite, where calcite dissolution occurs. For O_2 , only negligible consumption occur from oxidation of Fe(II) in the water and released from siderite dissolution.

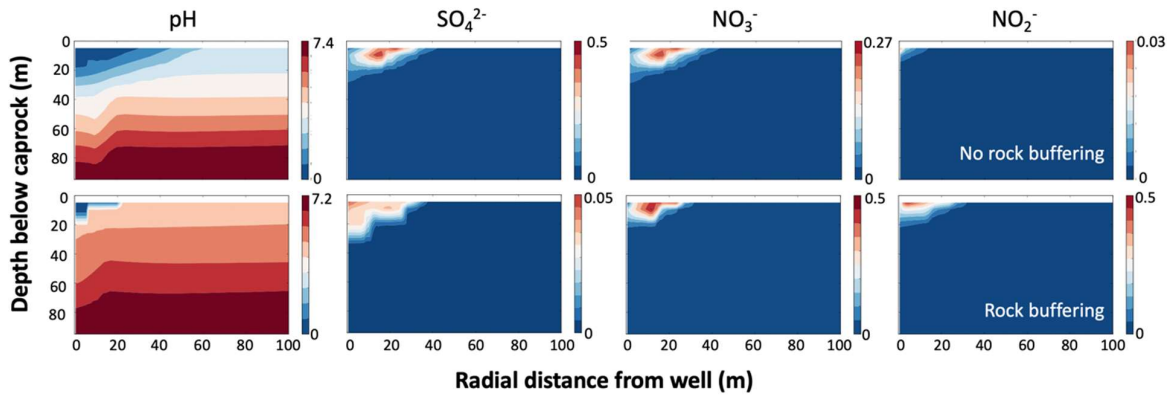


Figure 15. Calculated spatial distribution of pH, SO_4^{2-} , NO_3^- and NO_2^- from reactions of O_2 , SO_2 and NO_2 for the first 100 m radial distance from the well simulations of 0.1 Mt CO_2 per year for 10 years with or without rock-water interaction.

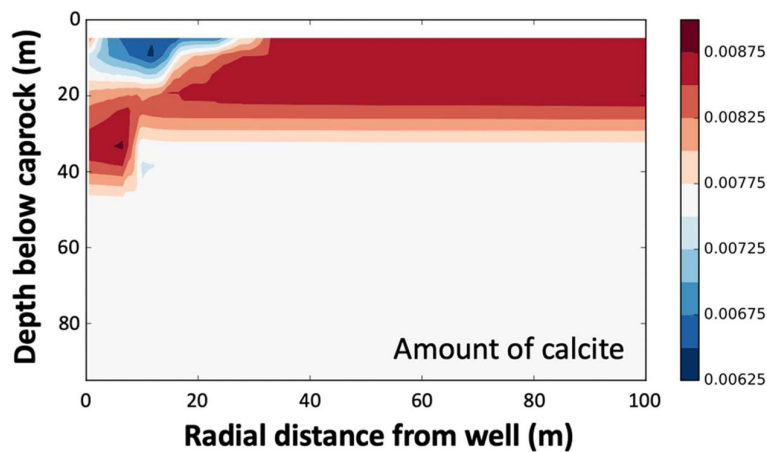


Figure 16. Calculated spatial distribution of calcite expressed as the fractional volume of cells for the first 100 m radial distance from well in the simulation of 0.1 Mt CO₂ per year for 10 years.

Importantly, pH is effectively buffered by calcite dissolution, meaning that the pH of cells influenced by impurities reaction remain close to the pH of ~4.6 generated by CO₂ dissolution. During the injection, only a small amount of calcite dissolves, roughly 15% (Figure 16). Thus, the rock effectively buffers the acid generated by the impurities' reaction. While the abundance of calcite varies in the formation, calculations with just siderite and K-feldspar results in minimum pH values that are not critically lower, pH 3.4. Thus, for the injection scenario modelled the acidification from impurities at the expected concentrations will most likely not pose a critical problem for the durability of infrastructure, neither is there reason to suspect the impurities will induce reactions to a degree that could cause the formation to lose its strength. However, we expect that impact of impurities on the reservoir properties could scale with the amount of impurities injected and the degree to which CO₂ is back produced, meaning that a separate set of calculations would be required for different injection strategies (i.e., several cycles of injection/production). Also, the alternating injection of oxidizing and reducing gas mixtures could change the outcome substantially. Finally, several potential reaction paths have not been included, because reactions constant do not to our knowledge exist for the reservoir conditions:

- i) Aqueous Fe(II) oxidation by O₂ can be catalyzed by mineral surfaces, such as iron oxides, speeding up the reaction (e.g., Tamura et al., 1976). The oxidation of aqueous Fe(II) would be likely to result in Fe(III)-oxide formation, a net reaction producing acid: $2 \text{Fe}^{2+} + 0.5 \text{O}_2 + 2 \text{H}_2\text{O} = \text{Fe}_2\text{O}_3 + 4 \text{H}^+$.
- ii) Data exists indicating that Fe(II) in siderite can reduce NO₂⁻ to N₂O at appreciable rates (Rakshit et al., 2008). However, the reaction rate appears to be decreasing with reaction time, potentially because of passivation of the siderite surface, making it complicated to embed in a reactive transport model.

4 Sensitivity study

As demonstrated in Sections 2 and 3.1.3.2, there are significant uncertainties in geological models for Stenlille and Havnsø, as well as in the experimental data on saturation functions. In the subsequent deliverables of the ConsenCUS project, the subsurface data for Stenlille and Havnsø will be re-processed using modern approaches as in (Bredesen, 2022). This will reduce corresponding uncertainties and will yield more accurate static and dynamic reservoir models for both sites.

In what follows, we focus on the uncertainty quantification for the saturation functions. Specifically, we consider the Brooks-Corey parametrization of the CO₂-water relative permeabilities and capillary pressures and characterize the behavior of the CO₂ recovery factor with regards to changes in the Brooks-Corey parameters using the design of experiments (DOE) approach (Montgomery, 2012).

4.1 Sampling the Brooks-Corey parameters

Given the large span of experimentally measured Brooks-Corey parameters for the drainage and imbibition branches of the relative permeability and capillary pressure functions (see Table 2 and Table 3), we assume that these parameters are uniformly distributed within the corresponding ranges. Then, we generate 100 quasi-random samples for each of the parameters

$$S_{wr}, S_{nrd}, S_{nri}, K_{wd}, K_{wi}, K_n, n_{wd}, n_{wi}, n_{nd}, n_{ni}, P_{ei}, P_{ed} - P_{ei}, \lambda_i, \lambda_d - \lambda_i \quad (9)$$

within the corresponding uncertainty ranges using the Latin hypercube sampling (LHS) approach (McKay, Beckman, & Conover, 1979).

The resulting relative permeability and capillary pressure curves are presented in Figure 17 and Figure 18, respectively. Notice that there is a significant number of sampled water relative permeabilities in Figure 17, which are characterized by a steep slope for large water saturations. However, there is only one experimental curve with this behavior in Figure 12. Moreover, this is exactly the curve which cannot be accurately represented with the Brooks-Corey parametrization, cf. Figure 13. Despite these discrepancies, we argue that the sampled saturation curves can be used to assess the impact of uncertainties in saturation functions on simulation results.

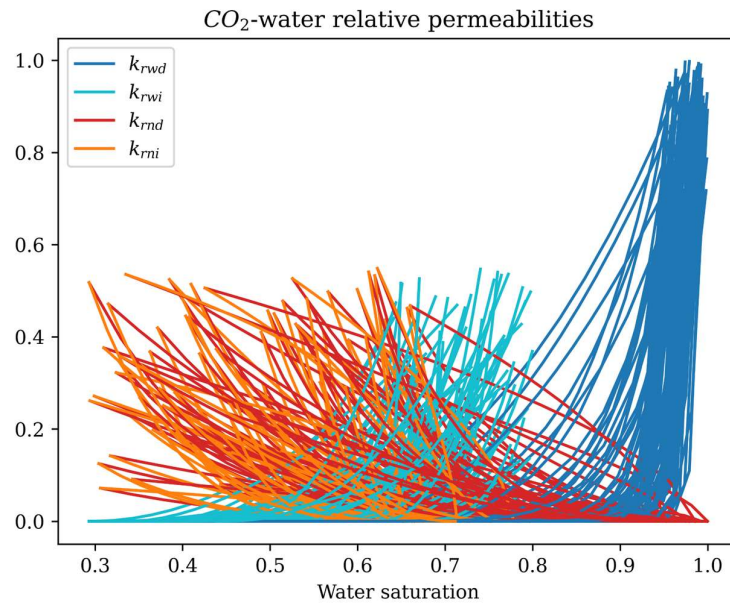


Figure 17. 100 realizations of Brooks-Corey relative permeability curves.

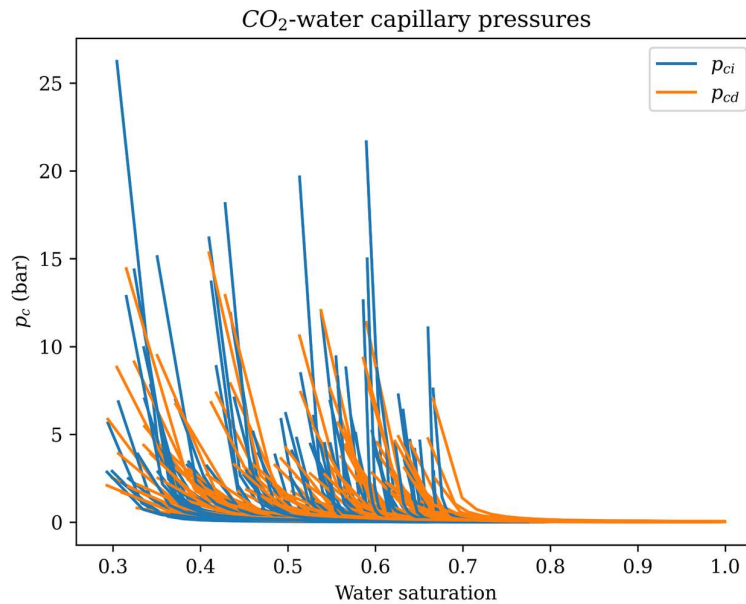


Figure 18. 100 realizations of Brooks-Corey capillary pressure curves.

4.2 Impact of saturation functions

4.2.1 Stenlille

Optimal well placement for temporary CO₂ storage implies that the injection/production wells are located at the top of the structure and are completed in high permeability and high porosity layers. The top zone of Stenlille structure near the well ST-11 satisfies these criteria as can be seen in Figure 6.

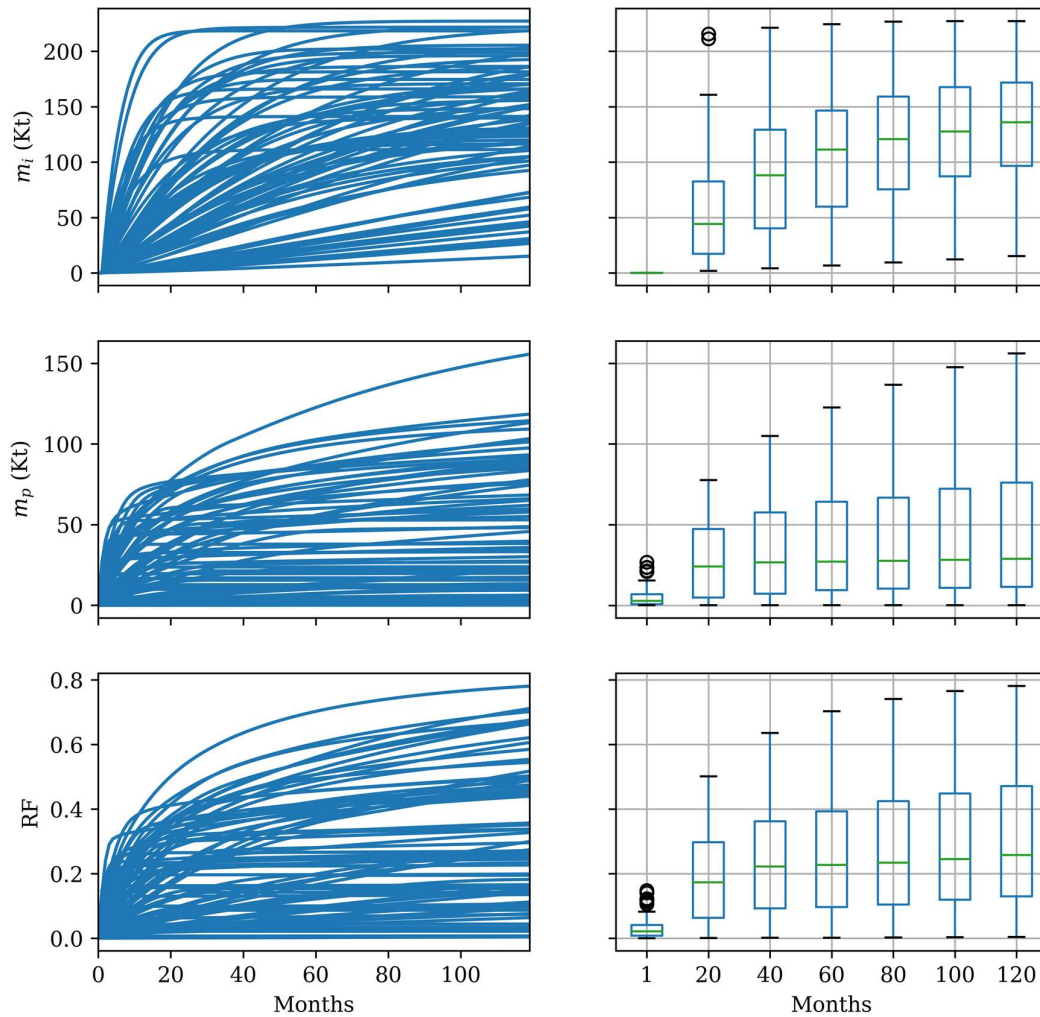


Figure 19. Efficiency of temporary CO₂ storage at Stenlille well ST-11 using an ensemble of saturation functions.

Consider a scenario, when CO₂ is injected in ST-11 for 10 years with the bottomhole pressure control of 257 bars (cf. Section 3.1.4), followed by 10 years production with the topside pressure

control of 1 bar. Depending on a specific set of relative permeabilities and capillary pressures in Figure 17 and Figure 18, the mass of injected and produced CO₂ varies as indicated in Figure 19.

In the left graphs of Figure 19, the ensemble of injected CO₂ mass in kilotons is plotted as a function of time after injection start, and the ensemble of produced CO₂ mass in kilotons, as well as the corresponding recovery factors, are plotted as a function of time after production start.

The distributions of injected and produced amounts and the CO₂ recovery factors are visualized using box plots in the right column of Figure 19Figure 22. The boxes extend from the first quartile (Q₁; 25% of the data is below this point) to the third quartile (Q₃; 75% of the data is below this point) values of the data, with a line at the median (Q₂; green line; 50% of the data is below this point). The outliers (denoted with circles) are defined as the data points, lying farther than $1.5 * (Q_3 - Q_1)$ from the edges of the box.

The box plots in Figure 19 highlight that there is a large spread in injected and produced amounts and in CO₂ recovery factors, depending on a particular choice of the saturation functions. After 10 years of injection in ST-11, the median injected mass is 135 Kt, whereas the first and third quartiles are 96 and 171 Kt, respectively. The spread in produced volumes is even larger, with median being 29 Kt, and first and third quartiles of 11 and 76 Kt, respectively.

The fact that the amount of the recovered CO₂ is always less than the amount of injected CO₂ (recovery factor, $RF < 1$) is due to capillary and solubility trapping. For the scenario in Figure 19, the median recovery factor is 0.25.

The uncertainty in injected and produced amounts and in CO₂ recovery factors is especially high at the beginning of production (up to month 4), where a significant number of outliers is present (circles in Figure 19).

4.2.2 Havnsø

Consider the case when CO₂ is injected in a vertical well, located at the top of the Havnsø structure, as indicated in Figure 7. Similar to the Stenlille case in Section 4.2.1, assume that CO₂ is injected for 10 years with the bottomhole pressure control of 246 bars (cf. Section 3.1.4), followed by 10 years production with the topside pressure control of 1 bar. The sensitivity of the mass of injected and produced CO₂ with regards to changes in Brooks-Core parameters (9) is presented in Figure 20.

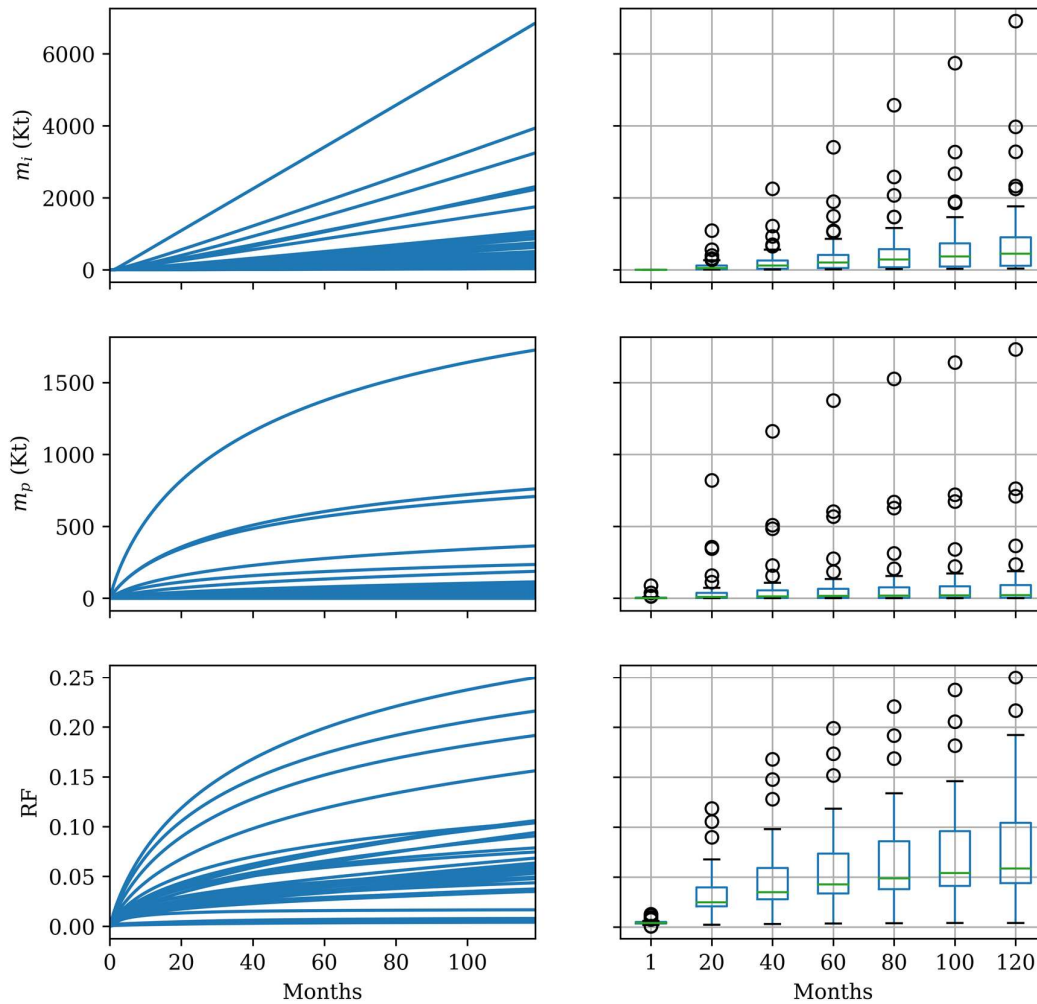


Figure 20. Efficiency of temporary CO₂ storage at Havnsø using an ensemble of saturation functions.

Observe that for Havnsø, the amount of injected CO₂ is considerably larger as compared to the top zone of Stenlille (cf. Figure 19), which is due to a much larger reservoir volume at Havnsø. However, the produced CO₂ amount and, consequently, the median recovery factor of 0.06 for Havnsø is smaller than the one for Stenlille ($RF = 0.25$ for the scenario in Figure 19). In line with (Kaufmann, Aavatsmark, Nøkleby, & Aurdal, 2016), this can be explained by the fact that unlike the top zone of Stenlille, the Havnsø is not compartmentalized and therefore the back-production of CO₂ due to pressure drive is relatively small.

4.3 Impact of wells location

Let us study the role of top reservoir topology and static reservoir properties on the CO₂ recovery factor. To this end, we simulate two scenarios with the same injection and production strategy, using the same realizations of the saturation functions, presented in Figure 17 and Figure 18, but for different Stenlille wells. Specifically, we consider the wells ST-11 and ST-01, perforated in the top reservoir zone. For both wells, CO₂ is injected for 10 years with the bottomhole pressure control of 257 bars (cf. Section 3.1.4), followed by 10 years production with the topside pressure control of 1 bar. For both scenarios, the snapshots of CO₂ saturation at the end of injection are presented in Figure 21.

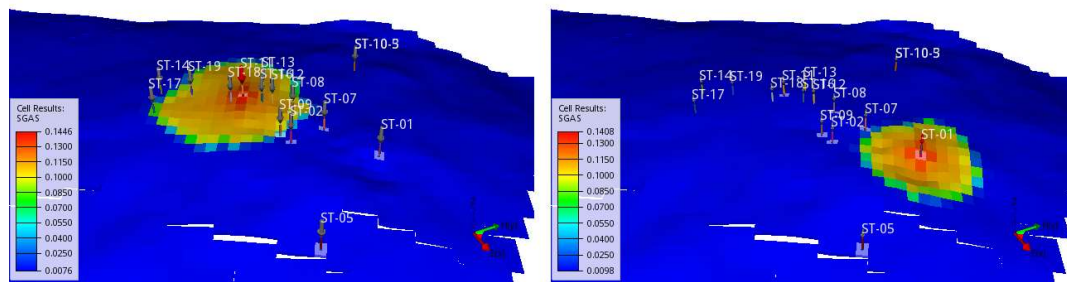


Figure 21. CO₂ saturations at the end of 10-year injection in the well ST-11 (left) and in the ST-01 (right).

Different CO₂ plume shapes in Figure 21 are due to different top reservoir topology and distributions of reservoir properties near the two wells. As can be seen in Figure 6, the region near ST-11 is characterized by higher permeability than near ST-01. Also, there is a hump near ST-11, which prevents the buoyant CO₂ to move away from the well. On the contrary, there is a slope in top reservoir surface near ST-01, which results in a slight shift of the CO₂ plume away from the well.

The sensitivity of CO₂ injection and production for ST-01 as a function of various saturation functions is presented in Figure 22. Observe that the amount of both the injected and produced CO₂ (median masses are 70 Kt and 15 Kt, respectively) is much lower as compared to the case of ST-11, see Figure 19. The reasons for this behavior are *i*) worse reservoir quality (i.e., lower porosity and permeability) near ST-01 as compared to ST-11 and *ii*) different topography near the two wells. These observations highlight the importance of detailed reservoir characterization for accurate estimates of reservoir productivity and injectivity.

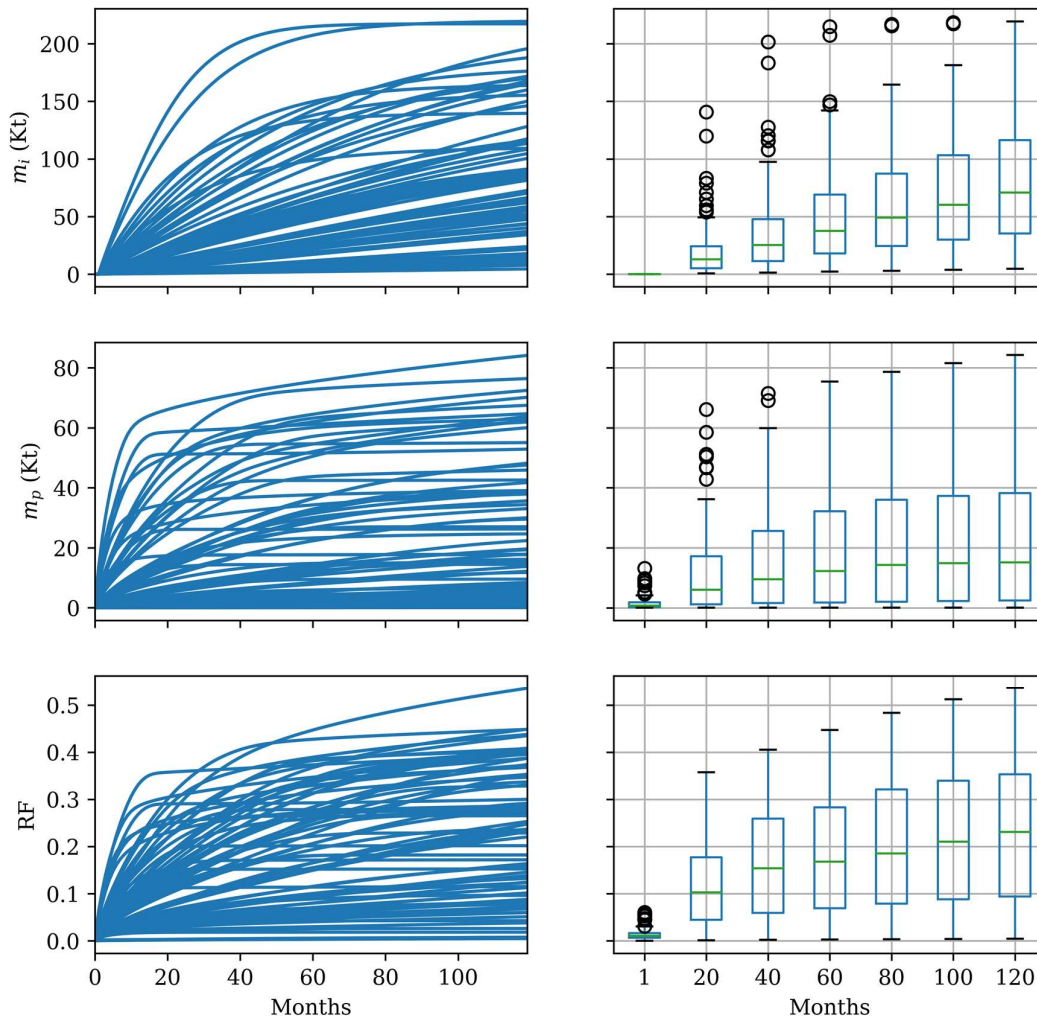


Figure 22. Efficiency of temporary CO₂ storage at Stenlille well ST-01 using an ensemble of saturation functions.

One might argue that the low CO₂ recovery in Figure 19 and Figure 22 is due to a relatively small amount of CO₂ injected. Thus, CO₂ saturation does not significantly exceed the critical saturation and much of the injected gas becomes immobile due to capillary trapping. Note that one cannot simply increase the injection rates because this will lead to increased reservoir pressures, eventually exceeding the fracturing pressures, cf. Section 3.1.4.

In order to inject more CO₂ while satisfying the fracturing pressure constraint, a natural approach is to use more injection wells. In what follows, we choose 6 neighbor wells (ST-01, ST-02, ST-07, ST-08, ST-09, ST-11) for injection under the same bottomhole-pressure constraint of 257 bars. A snapshot of CO₂ saturation after the injection stop is presented in Figure 23.

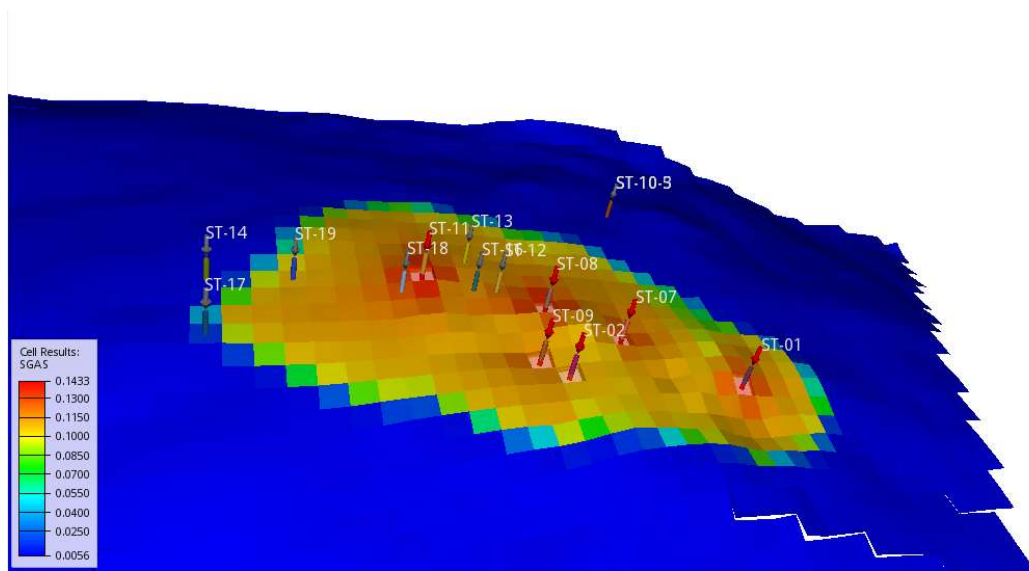


Figure 23. CO₂ saturation at the end of 10-year injection in the 6 neighbor wells at Stenlille.

As expected, CO₂ occupies a larger part of the reservoir, as compared to injection in one well only, cf. Figure 21. The efficiency of temporary CO₂ storage for this injection/production scenario is presented in Figure 24. The median mass of injected CO₂ is 149 Kt, cf. with 135 Kt for injecting in ST-11 only (see Section 4.2.1) and with 70 Kt in ST-01 only. The joint injected CO₂ from 6 wells is less than injected mass from separate wells because injection pressurizes the reservoir, and the overall injection rate is reduced in order to satisfy the fracturing pressure constraint.

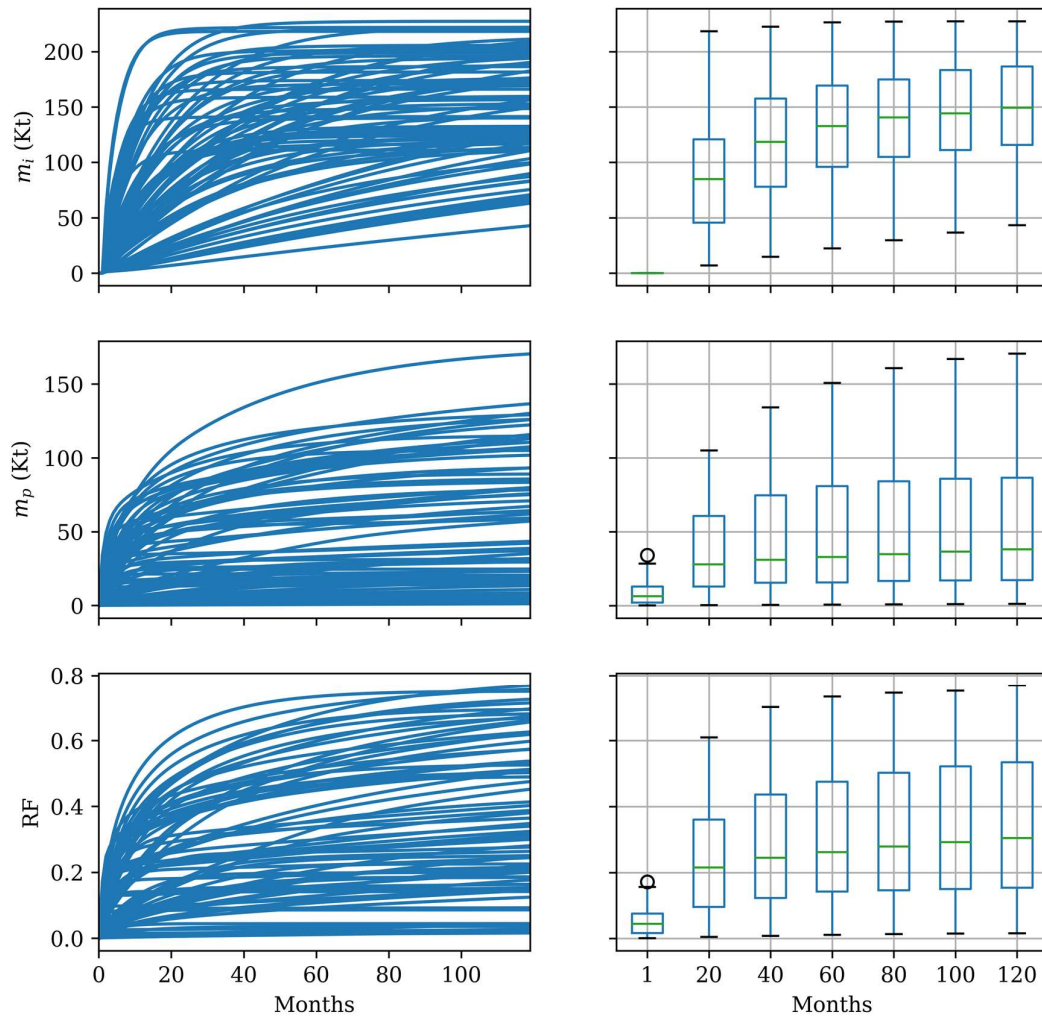


Figure 24. Efficiency of temporary CO₂ storage at Stenlille by injection and production using 6 neighbor wells, depicted in Figure 23.

5 Conclusions

Permanent and temporary CO₂ storage in saline aquifers is associated with uncertainties, which might affect the efficiency and safety of storage operations. Taking as an example two saline aquifers in the Danish area – Stenlille and Havnsø – we demonstrate that fluid-rock interactions play a major role in estimating the CO₂ storage capacity and the CO₂ recovery efficiency. The safety requirements with regards to seal integrity impose a limit on CO₂ injection rates. For the top zone of Stenlille, this constraint limits the injection rates to 150 Kt over the period of 10 years. For Havnsø, modelling results suggest that one can safely inject 449 Kt without risk of fracturing.

In all considered cases, the median recovery factor (i.e., the ratio of produced amount of CO₂ to injected) is not more than 0.3. This means that temporary CO₂ storage can never be feasible without permanently storing a large (>60%) fraction of injected CO₂. Note that this estimate is qualitatively similar to the case of natural gas storage in saline aquifers.

Insufficient experimental data lead to considerable uncertainties in estimating the parameters of the rock-fluid interaction, which are described by saturation functions – the relative permeabilities and capillary pressures. Consequently, all conclusions in this work are provided in terms of statistical estimates. Future work will include dedicated laboratory experiments targeted at reducing of these uncertainties.

The results of geochemical modelling demonstrate that although the fractional abundance of salt precipitation in the pore space is relatively modest for most modelled parameter sets, we cannot exclude that salt formation could pose a problem. The acidification from impurities at the expected concentrations will most likely not pose a critical problem for the durability of infrastructure, neither is there reason to suspect the impurities will induce reactions to a degree that could cause the formation to lose its strength. However, the impact of impurities on the reservoir properties could scale with the amount of impurities injected, meaning that a separate set of calculations would be required for different injection strategies (i.e., several cycles of injection/production).

6 Bibliography

- Akbarabadi, M., & Piri, M. (2013). Relative permeability hysteresis and capillary trapping characteristics of supercritical CO₂/brine systems: An experimental study at reservoir conditions. *Advances in Water Resources*.
- Allen, R., Nilsen, H. M., Lie, K.-A., Møyner, O., & Andersen, O. (2018). Using simplified methods to explore the impact of parameter uncertainty on CO₂ storage estimates with application to the Norwegian Continental Shelf. *International Journal of Greenhouse Gas Control*.
- Bahadori, A., Vuthaluru, H. B., & Mokhatab, S. (2009). New correlations predict aqueous solubility and density of carbon dioxide. *International Journal of Greenhouse Gas Control*.
- Bear, J., & Cheng, A. (2010). *Modeling Groundwater Flow and Contaminant Transport*. Dordrecht, The Netherlands: Springer.
- BEIS. (2018). *Shipping CO₂: UK Cost Estimation Study*. Department for Business, Energy and Industrial Strategy (BEIS).
- Bennion, B., & Bachu, S. (2005). Relative Permeability Characteristics for Supercritical CO₂ Displacing Water in a Variety of Potential Sequestration Zones. Society of Petroleum Engineers.
- Bennion, D. B., & Bachu, S. (2006). Supercritical CO₂ and H₂S - Brine Drainage and Imbibition Relative Permeability Relationships for Intercrystalline Sandstone and Carbonate Formations. Society of Petroleum Engineers.
- Benson, S., Pini, R., Reynolds, C., & Krevor, S. (2013). *Relative Permeability Analysis to Describe Multi-Phase Flow in CO₂ Storage Reservoirs*. Global CCS Institute. Retrieved from <https://www.globalccsinstitute.com/archive/hub/publications/111691/relative-permeability-analysis-describe-multi-phase-flow-co2-storage-reservoirs.pdf>
- Bredesen, K. (2022). Assessing rock physics and seismic characteristics of the Gassum Formation in the Stenlille aquifer gas storage – A reservoir analog for the Havnsø CO₂ storage prospect, Denmark. *International Journal of Greenhouse Gas Control*.
- Brooks, R., & Corey, A. (1964). Hydraulic Properties of Porous Media. *Hydrology Papers*.
- Cavanagh, A. J. (2015). The Sleipner CO₂ storage site: using a basin model to understand reservoir simulations of plume dynamics. *First Break*.
- Chang, Y.-B., Coats, B. K., & Nolen, J. S. (1998). *A Compositional Model for CO₂ Floods Including CO₂ Solubility in Water*. Society of Petroleum Engineers.

- Crotogino, F. (2022). Traditional bulk energy storage—coal and underground natural gas and oil storage. *Storing energy*, 633-649.
- Dake, L. P. (1978). *Fundamentals of reservoir engineering*. Elsevier.
- DONG. (2013). *Miljøregnskab*. DONG Energy.
- Dusseault, M. R. (2002). Sequestration of CO₂ in Salt Caverns. *Canadian International Petroleum Conference*. Calgary, Alberta.
- Fenghour, A., Wakeham, W. A., & Vesovic, V. (1998). The Viscosity of Carbon Dioxide. *Journal of Physical and Chemical Reference Data*.
- Frykman, P. (2020). *3D static reservoir model of the Havnsø structure*. Geological Survey of Denmark and Greenland (GEUS).
- Global CCS Institute. (2021). *Global Status of CCS 2021*. Global CCS Institute.
- GSD. (2017). *Årsrapport*. Gas Storage Denmark.
- Han, W. S., Kim, K.-Y., Esser, R. P., Park, E., & McPherson, B. J. (2011). Sensitivity Study of Simulation Parameters Controlling CO₂ Trapping Mechanisms in Saline Formations. *Transport in Porous Media volume*.
- Hjelm, L., Anthonsen, K., Dideriksen, K., Møller Nielsen, C., Nielsen, L., & Mathiesen, A. (2020). *Evaluation of the CO₂ storage potential in Denmark*. Geological Survey of Denmark and Greenland (GEUS). Retrieved from [https://www.geus.dk/Media/637599867373909761/Evaluation%20of%20the%20CO2%20storage%20potential%20in%20Denmark%20\(GEUS%20rapport%202020_46\).pdf](https://www.geus.dk/Media/637599867373909761/Evaluation%20of%20the%20CO2%20storage%20potential%20in%20Denmark%20(GEUS%20rapport%202020_46).pdf)
- Holmslykke, H. D., Olivarius, M., Kjøller, C., & Dideriksen, K. (2020). *Reservoir characterisation and hydrogeochemical reactions between CO₂ and reservoir rock*. Geological Survey of Denmark and Greenland (GEUS).
- IEA. (2019). *Putting CO₂ to Use*. International Energy Agency.
- IPCC. (2005). *Carbon Dioxide Capture and Storage*. Cambridge, United Kingdom: Cambridge University Press.
- IPCC. (2013). Summary for policymakers. In Q. D.-K. Stocker TF (Ed.), *Climate change 2013: the physical science basis*. Cambridge: Cambridge University Press.
- IPCC. (2022). *Climate Change 2022: Impacts, Adaptation and Vulnerability*. IPCC.
- Jackson, S. J., & Krevor, S. (2020). Small-scale capillary heterogeneity linked to rapid plume migration during CO₂ storage. *Geophysical Research Letters*.
- Jensen M. (2014). *Operational flexibility of CO₂ transport and storage*. Pittsburgh, PA: U.S. Department of Energy.
- Juanes, R., Spiteri, E. J., Orr, F. M., & Blunt, M. J. (2006). Impact of relative permeability hysteresis on geological CO₂ storage. *Water Resources Research*.
- Jung, Y., Pau, G. S., S., F., & C., D. (2018). TOUGH3 User's Guide. Lawrence Berkeley National Laboratory.

- Kaufmann, R., Aavatsmark, I., Nøkleby, P. H., & Aurdal, T. A. (2016). Using an aquifer as CO₂ buffer storage. *International Journal of Greenhouse Gas Control*.
- Kjøller, C., Weibel, R., Bateman, K., Laier, T., Nielsen, L. H., Frykman, P., & Springer, N. (2011). Geochemical impacts of CO₂ storage in saline aquifers with various mineralogy—Results from laboratory experiments and reactive geochemical modelling. *Energy Procedia*, 4724-4731.
- Koenen, M. a. (2018). Seasonal CO₂ Storage in Q16-Maas, The Netherlands. *14th Greenhouse Gas Control Technologies Conference*. Melbourne, Australia.
- Kristensen, L. (2020). *Reservoir data – Stenlille area*. Geological Survey of Denmark and Greenland (GEUS).
- Laier, T., & Øbro, H. (2009). Environmental and safety monitoring of the natural gas underground storage at Stenlille, Denmark. *Underground Gas Storage: Worldwide Experiences and Future Development in the UK and Europe*. Geological Society of London.
- Manceau, J., & Rohmer, J. (2016). Post-injection trapping of mobile CO₂ in deep aquifers: Assessing the importance of model and parameter uncertainties. *Computational Geosciences*.
- Marini, L. (2006). *Geological Sequestration of Carbon Dioxide*. Elsevier.
- Mathiesen, A., Laghari, S., & Rasmussen, R. (2020). *Depth conversion of seal and reservoir maps from the Havnsø and Hanstholm areas*. Geological Survey of Denmark and Greenland (GEUS).
- McKay, M. D., Beckman, R. J., & Conover, W. J. (1979). A Comparison of Three Methods for Selecting Values of Input Variables in the Analysis of Output from a Computer Code. *Technometrics*.
- Millero, F. J., Sotolongo, S., & Izaguirre, M. (1987). The oxidation kinetics of Fe(II) in seawater. *Geochimica et Cosmochimica Acta*, 51, 793-801.
- Miri, R., & Hellevang, H. (2016). Salt precipitation during CO₂ storage - A review. *International Journal of Greenhouse Gas Control*.
- Möller, D. (1988). Kinetic model of atmospheric SO₂ oxidation based on published data. *Atmospheric Environment*.
- Montgomery, D. C. (2012). *Design and Analysis of Experiments*. Wiley.
- Morgan, B., & Lahav, O. (2007). The effect of pH on the kinetics of spontaneous Fe(II) oxidation by O₂ in aqueous solution – basic principles and a simple heuristic description. *Chemosphere*, 68, 2080–2084.
- Mualem, Y. (1976). A new model for predicting the hydraulic conductivity of unsaturated porous media. *Water Resources Research*.

- Ott, H., Roels, S., & De Kloe, K. (2015). Salt precipitation due to supercritical gas injection: I. Capillary-driven flow in unimodal sandstone. *International Journal of Greenhouse Gas Control*.
- Palandri, J. L., & Kharaka, Y. K. (2004). *A compilation of rate parameters of water-mineral interaction kinetics for application to geochemical modeling*. U.S. Geological Survey. Retrieved from <https://pubs.usgs.gov/of/2004/1068>
- Park, J. Y., & Lee, Y. N. (1988). Solubility and decomposition kinetics of nitrous acid in aqueous solutions. *Journal of Physical Chemistry*.
- Parkhurst, D. L., & Appelo, C. A. (2013). Description of input and examples for PHREEQC. Version 3 – A computer program for speciation, batch-reaction, one-dimensional transport, and inverse geochemical calculations. U.S. Geological Survey.
- Peysson, Y. A. (2014). Well injectivity during CO₂ storage operations in deep saline aquifers—part 1: experimental investigation of drying effects, salt precipitation and capillary forces. *International Journal of Greenhouse Gas Control*.
- Pini, R., Krevor, S. C., & Benson, S. M. (2012). Capillary pressure and heterogeneity for the CO₂/water system in sandstone rocks at reservoir conditions. *Advances in Water Resources*.
- Pruess, K. (2005). ECO2N: A TOUGH2 Fluid Property Module for Mixtures of Water, NaCl, and CO₂.
- Pruess, K. (2009). Formation dry-out from CO₂ injection into saline aquifers: 2. Analytical model for salt precipitation. *Water Resources Research*.
- Rakshit, S., Matocha, C. J., & Coyne, M. S. (2008). Nitrite reduction by siderite. *Soil Science Society of America Journal*, 72, 1070-1077.
- Ringrose, P. (2020). *How to Store CO₂ Underground: Insights from early-mover CCS Projects*. Springer.
- Rütters, H., Fischer, S., Hoa, L. Q., Bettge, D., Bäßler, R., Maßmann, J., . . . Svensson, K. (2022). Towards defining reasonable minimum composition thresholds – Impacts of variable CO₂ stream compositions on transport, injection and storage. *International Journal of Greenhouse Gas Control*.
- Sarkarfarshi, M., Malekzadeh, F. A., Gracie, R., & Dusseault, M. B. (2014). Parametric sensitivity analysis for CO₂ geosequestration. *International Journal of Greenhouse Gas Control*.
- Schlumberger. (2017). Eclipse Technical Description.
- Selosse, S., & Ricci, O. (2017). Carbon capture and storage: Lessons from a storage potential and localization analysis. *Applied Energy*.
- Spitz, T. (2018). On the variability of CO₂ feed flows into CCS transportation and storage networks. *International Journal of Greenhouse Gas Control*.

- Squadrito, G. L., & Postlethwait, E. M. (2009). On the hydrophobicity of nitrogen dioxide: Could there be a “lens” effect for NO₂ reaction kinetics? . *Nitric Oxide*.
- Talman, S. (2015). Subsurface geochemical fate and effects of impurities contained in a CO₂ stream injected into a deep saline aquifer: What is known. *International Journal of Greenhouse Gas Control*.
- Tamura, H., Goto, K., & Nagayama, M. (1976). The effect of ferric hydroxide on the oxygenation of ferrous ions in neutral solution. *Corrosion Science*, 16, 197-207.
- US DoE. (2017). *Accelerating Breakthrough Innovation in Carbon Capture, Utilization, and Storage*. Houston, Texas: Mission Innovation Carbon Capture, Utilization, and Storage (CCUS) Expert’s Workshop.
- van Genuchten, M. (1980). A Closed-form Equation for Predicting the Hydraulic Conductivity of Unsaturated Soils. *Soil Science Society of America Journal*.
- Wang, J., Li, J., Ye, J., Zhao, J., Wu, Y., Hu, J., . . . Zhang, Q. (2020). Fast sulfate formation from oxidation of SO₂ by NO₂ and HONO observed in Beijing haze. *Nature Communications*.
- Wangen, M. (2002). Effective permeability of hydrofractured sedimentary rocks. (A. G. Koestler, & R. Hunsdale, Eds.) *Norwegian Petroleum Society Special Publications*.
- Weibel, R., Kjølter, C., Bateman, K., Nielsen, L., Frykman, P., Springer, N., & Laier, T. (2011). Mineral changes in CO₂ experiments — Examples from Danish onshore saline aquifers. *Energy Procedia*, 4495-4502.
- Xu, T., Sonnenthal, E., Spycher, N., & Zheng, L. (2017). TOUGHREACT V3.32 Reference Manual: A Parallel Simulation Program for Non-Isothermal Multiphase Geochemical Reactive Transport V3.32 Reference Manual. Lawrence Berkeley National Laboratory. University of California, Berkeley, CA. Lawrence Berkeley National Laboratory.
- Xu, T., Spycher, N., Sonnenthal, E., Zhang, G., Zheng, L., & Pruess, K. (2011). TOUGHREACT Version 2.0: a simulator for subsurface reactive transport under non-isothermal multiphase flow conditions. *Computational Geosciences*.
- Zoback, M. D. (2007). *Reservoir Geomechanics*. Cambridge University Press.